Linear Accelerator Technology

D. Alesini
Laboratori Nazionali di Frascati dell'INFN, Frascati, Italy

Abstract

The expression 'linear accelerator technology' usually addresses all technological topics related to linear accelerators' (linac) realization. These topics comprise, for instance, accelerating structures, Radio Frequency (RF) sources, magnets, diagnostics systems, controllers, power supplies, vacuum systems, particle sources, etc. Obviously, the extent of all these subjects is too wide to be covered in a single one-hour lecture and, therefore, this paper will only present an overview of the RF structures (including their fabrication technology) with a few examples of particle sources, RF sources and waveguide components. Moreover, the focus will be on linac technology for Free-Electron Lasers (FELs) and Energy Recovery Lasers (ERLs), which are electron accelerators. Electrons, in fact, even at very low energies (a few MeV) travel very close to the speed of light, and this fact has a direct consequence in the accelerating structures design, since they can be identical all along the linac.

Keywords:

Radio Frequency; particle accelerators; cavity; electromagnetic field; superconductivity; linac.
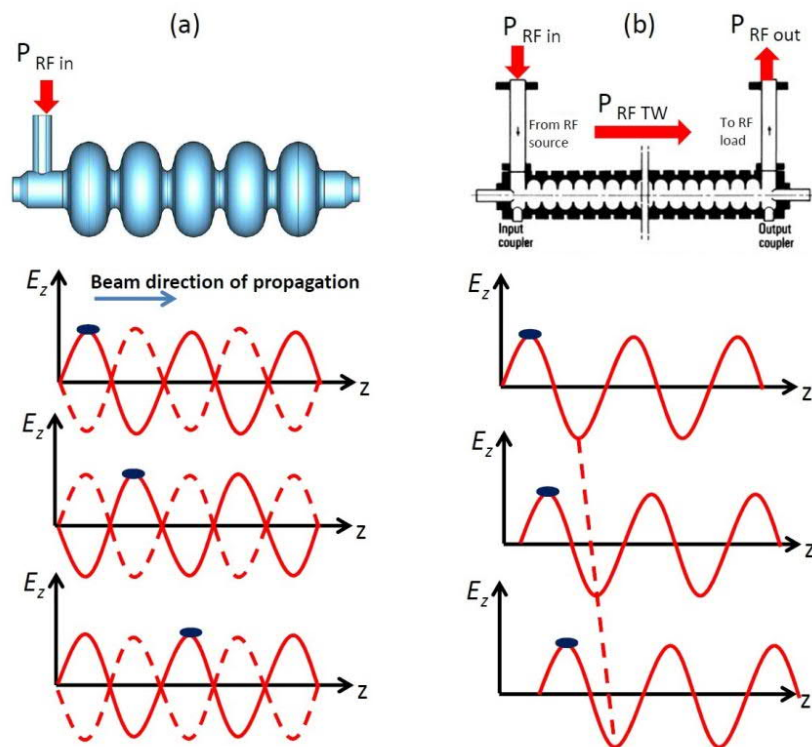
1   Accelerating structures

To accelerate charged particles, Electromagnetic (EM) fields are used. This method is effective only if, however, there is a component of the electric field along the direction of propagation of the particles. In common practice, this particular configuration is obtained with two different solutions, schematically represented in Fig. 1.

i) Using Standing Wave (SW) TM_{010}-like modes in a resonant cavity (or multiple resonant cavities), in which the beam's passage in the cavities is synchronous with the resonating field. The electric field oscillates in each cell at a given frequency (from hundreds of megahertz to several gigahertz) and it is synchronous with the bunches' passage in each cell, so that the beam will experience a net accelerating gradient. A single coupler feeds the structure, as will be described below.

ii) Using Travelling Wave (TW) TM_{01}-like modes in a disk-loaded structure, in which the RF wave co-propagates with the beam with a phase velocity equal to the beam velocity ($\sim c$ for relativistic electrons). The power flows into the structure through an input coupler, and is collected and dissipated at the end of the section by an output coupler connected to an RF load, to avoid reflections that can strongly affect the beam dynamics and might damage the RF power source, as will be described below.

The structures can be made of different materials: copper (Cu) for Normal Conducting (NC) cavities and niobium (Nb) for Superconducting (SC) cavities; and are powered by RF generators (e.g. klystrons, solid-state amplifiers). The choice between the NC and the SC technologies depends on the machine's required performance:

i) Average accelerating field.

ii) RF pulse length, which is directly related to the bunch train length that it is possible to accelerate: from a few μs to hundreds of ms up to a continuous wave (CW) operation.

iii) Repetition rate (i.e. the number of RF pulses that feed the structures in one second). In this regard, it is useful to define the Duty Cycle (DC) as the ratio between the RF pulse length and its period. Low DC accelerators (DC=10^{-3} to 10^{-5}) operate in a pulsed regime with very short RF pulses (~μs) and a relatively low repetition rate (10 Hz to 100 Hz). On the contrary, high DC machines (DC>10^{-3}) operate with long RF pulses (>ms) up to CW operation (i.e. DC=1).

iv) Average beam current (from μA to hundreds of mA).

v) Available space, etc.

Typically, NC structures are employed in pulsed low DC Free-Electron Laser (FEL) linacs while SC structures are used for long RF pulses and high DC FEL linacs or Energy Recovery Lasers (ERLs).

Fig. 1: Acceleration principle using (a) SW or (b) TW structures. In a SW cavity the cell length has to be equal to half the wavelength of the RF field (for π-mode structures). In this way, the bunch in each cell is always synchronous with the electric field positive half-wave. In a TW structure the EM field travels together with the bunch, continuously transferring its energy to the particles. If the bunch velocity matches the EM wave velocity this transfer is obviously maximized.

2   Standing wave cavities

Before comparing different accelerating technologies, it is necessary to define a set of parameters useful for characterizing the various structures. Let us start with SW cavities.

These are metallic, closed volumes where the EM field has very well-defined spatial configurations (resonant modes) whose components, including the accelerating field on axis (E_z) rigidly oscillates at a specific frequency called the resonant frequency (f_{res}). The modes are excited coupling RF

generators to the cavity through waveguides or coaxial cables. The resonant modes are called SW modes because they have a spatial configuration that is fixed, and oscillate in time. For a SW cavity the accelerating field on the axis can be written as

$$E_z(z,t) = E_{RF}(z)\cos\left(\underbrace{2\pi f_{RF} t + \varphi}_{\omega_{RF}}\right) = \text{Real}\left[\tilde{E}_z(z) e^{j\omega_{RF}t}\right] \qquad (1)$$

where f_{RF} is the excitation frequency of the generator equal to (or close to) the resonant frequency of the cavity, ω_{RF} is the angular excitation frequency, $E_{RF}(z)$ (or the phasor $\tilde{E}_z$) is a real (complex) function related to the spatial configuration of the mode.

For a pure cylindrical structure (usually called a 'pillbox cavity') the first accelerating mode (i.e. the mode with non-zero longitudinal electric field on the axis) is the TM_{010} mode. It has a well-known analytical solution from Maxwell's equations, and its spatial configuration is given in Fig. 2. For this mode the electric field has a longitudinal component only, while the magnetic one is purely azimuthal. The corresponding complex phasors are given by [1, 2]

$$\begin{cases} \tilde{E}_z = AJ_0\left(p_{01}\dfrac{r}{a}\right) \\ \tilde{H}_\theta = -jA\dfrac{1}{Z_0}J_0'\left(p_{01}\dfrac{r}{a}\right) \end{cases} \qquad (2)$$

where a is the cavity radius, A is the mode amplitude and p_{01} (= 2.405) is the first zero of the Bessel function $J_0(x)$. The resonant frequency of this mode is given by: $f_{res} = \dfrac{p_{01}c}{2\pi a}$.
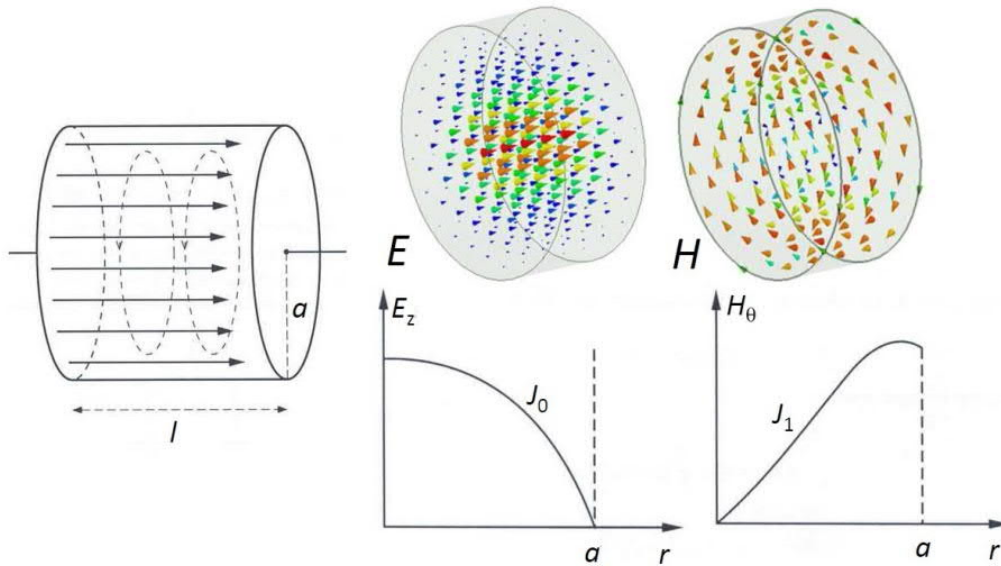
Fig. 2: TM_{010} accelerating mode of a pillbox cavity

The geometry of real cylindrical cavities is somewhat different to that of a pillbox. In fact, one has to also consider the perturbation introduced by the beam pipe, the power couplers to RF generators and any antenna or pick-up used to monitor the accelerating field inside the cavity. For this reason, the actual accelerating mode is called the TM_{010}-like mode.

Nowadays, real cavities and their couplers to the RF generators are designed using numerical codes that solve the Maxwell equations with the proper boundary.

A sketch of a cavity fed through a loop or a coaxial probe to an external generator is given in Fig. 3, where there are also reported the electric and magnetic field lines and the longitudinal electric field profile on the axis. Details of the coupler design can be found in [3].
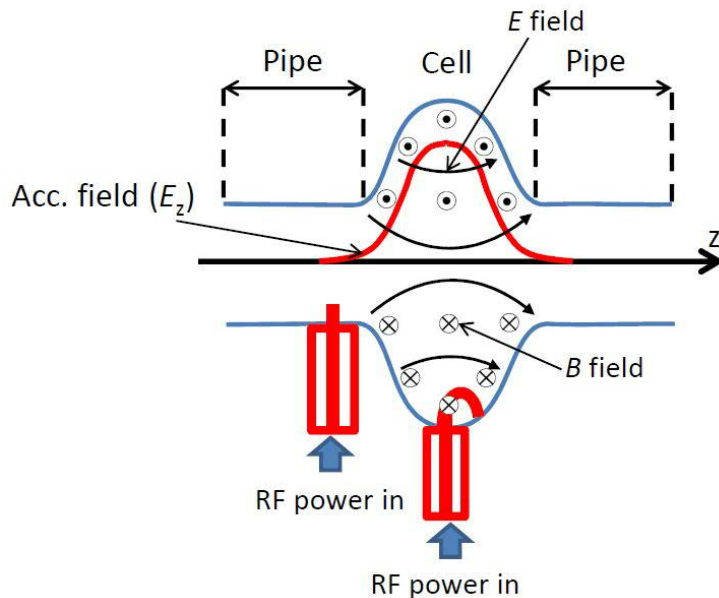

Fig. 3: Sketch of a real cavity operating on the TM$_{010}$-like mode with two type of coaxial couplers

2.1 Standing wave cavity parameters

To define the cavity parameters, we suppose that it is excited with a pure sinusoidal tone at f_{RF}. The maximum energy gain per unit charge (i.e. the accelerating voltage V_{acc}) of a particle crossing the cavity at a velocity v is obtained by integrating the time-varying accelerating field sampled by the charge along the trajectory

$$V_{acc} = \left| \int_{cavity} \tilde{E}_z(z) e^{j\omega_{RF}\frac{z}{v}} dz \right| \tag{3}$$

Real cavities have losses. Surface currents experience a surface resistance R_s and dissipate energy, so that a certain amount of RF power must be provided from outside to keep the accelerating field at the desired level. The total average dissipated power P_{diss} is given by

$$P_{diss} = \int_{\substack{cavity \\ wall}} \overbrace{\frac{1}{2} R_s \left| \tilde{H}_{tan} \right|^2}^{power\ density} dS \tag{4}$$

where $\tilde{H}_{tan}$ is the tangential magnetic field components on the surface. The value of the surface resistance depends on several factors, such as frequency and cavity material. As an example, at 1 GHz for a NC cavity in copper $R_s \cong 8$ mΩ while, for a SC cavity made in niobium at 2 K, $R_s \cong 10$ nΩ.

For a SW cavity the first figure of merit is the shunt impedance defined by

$$R = \frac{V_{acc}^2}{P_{diss}} \qquad [\Omega] \tag{5}$$

This parameter qualifies the efficiency of the cavity: the higher its value, the larger is the achievable accelerating voltage for a given dissipated power. Traditionally, it is the quantity to optimize in order to maximize the accelerating field for a given dissipated power. As an example, at 1 GHz for a NC single cell cavity a typical shunt impedance is of the order of 2 MΩ, while a SC single cell cavity at the same frequency is of the order of 1 TΩ, due to the extremely lower dissipated power.

The total energy (W) stored in the cavity is given by

$$W = \int_{\substack{\text{cavity} \\ \text{volume}}} \overbrace{\left(\frac{1}{4}\varepsilon \left| \vec{E} \right|^2 + \frac{1}{4}\mu \left| \vec{H} \right|^2 \right)}^{\text{energy density}} dV \tag{6}$$

The quality factor of the accelerating mode is then defined by the ratio of the cavity stored energy and the dissipated power on the cavity walls

$$Q_0 = \omega_{RF} \frac{W}{P_{diss}} \tag{7}$$

For a NC cavity operating at 1 GHz the quality factor is of the order of 10^4 while, for an SC cavity, values of the order 10^9 to 10^{10} can be achieved.

It can be easily demonstrated that the ratio R/Q is a pure geometric factor and it does not depend upon the cavity wall conductivity or operating frequency. This is the reason why it is always taken as a geometric design qualification parameter. The R/Q of a single cell is of the order of 100.

2.2 Standing wave cavity equivalent circuit

The quantities described above play crucial roles in the evaluation of the cavity performances. Let us consider a cavity powered by a source (klystron) at a constant frequency f_{RF} in CW and at a fixed power (P_{in}) as shown in Fig. 4. It can be demonstrated that the equivalent circuit of this system is that of a parallel RLC resonant circuit, as reported in Fig. 4. In the equivalent circuit the resistance R is exactly the shunt impedance of the cavity, and the quality factor is the quality factor of the RLC circuit. The transformer models the coupling between the waveguide and the cavity. With simple calculations, it is easy to demonstrate that the maximum accelerating voltage V_{acc} for a given input power P_{in} is given by

$$V_{acc} = \frac{\dfrac{2\sqrt{\beta}}{(1+\beta)}}{\sqrt{1+(Q_L\delta)^2}} \sqrt{RP_{in}} \tag{8}$$

where β is the generator–cavity coupling coefficient [3], $Q_L = Q_0/(1+\beta)$ is the loaded quality factor and $\delta = (f_{RF}/f_{res} - f_{res}/f_{RF})$.
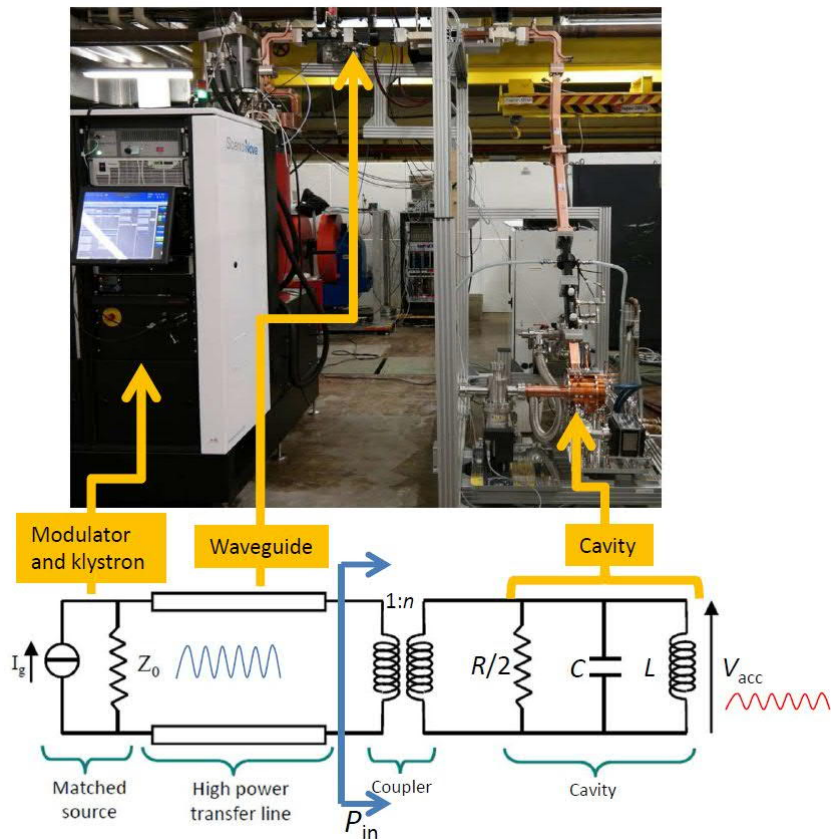
Fig. 4: Equivalent circuit of a cavity fed by a generator
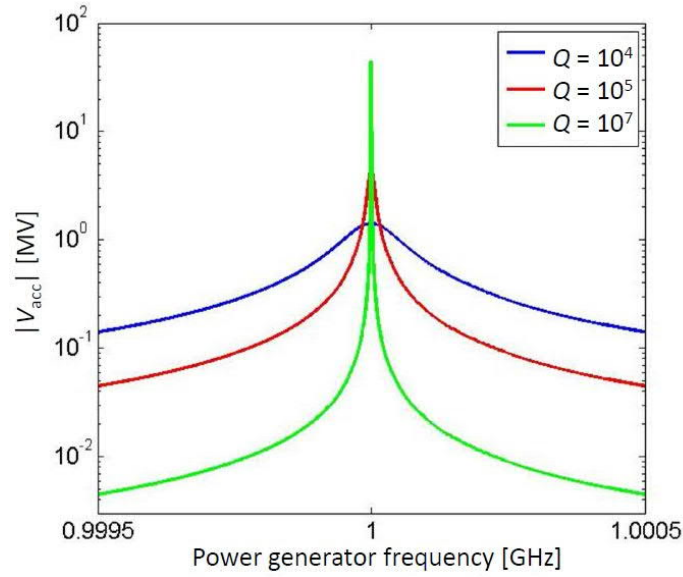
The dissipated power into the cavity is given by:

$$P_{diss} = \frac{\dfrac{4\beta}{(1+\beta)^2}}{1+(Q_L\delta)^2} P_{in} \tag{9}$$

The plot of the accelerating voltage as a function of the excitation frequency is given in Fig. 5 for three different values of the cavity quality factor supposing $P_{in} = 1$ MW, $R/Q = 100$ and $\beta = 1$ (critical coupling), and $f_{res} = 1$ GHz.

From previous formulas we easily see that, at the resonant frequency and in the case $\beta = 1$, we have

$$V_{acc} = \sqrt{RP_{in}} = \sqrt{\left(\frac{R}{Q}\right)Q_0 P_{in}} \tag{10}$$

This means that, for a given cavity, the accelerating voltage is proportional to $\sqrt{Q_0}$.

Fig. 5: Accelerating voltage as a function of the excitation frequency for a cavity with $R/Q = 100$, $\beta = 1$, $f_{res} = 1$ GHz, supposing that $P_{in} = 1$ MW.

On the other hand, the bandwidth of the resonance, defined as the δ-frequency interval corresponding to the points with an average dissipated power in the cavity of a factor of two lower than the dissipated power at resonance, is inversely proportional to the cavity quality factor according to the formula

$$\frac{\Delta f_{RF}|_{3dB}}{f_{res}} = \frac{1}{Q_L} \qquad \Rightarrow \qquad \begin{cases} \Delta f_{RF}|_{3dB}\Big|_{NC} \cong 100 kHz \\[2mm] \Delta f_{RF}|_{3dB}\Big|_{SC} < 1 Hz \end{cases} \tag{11}$$

The bandwidth of the cavity is, also, labeled 3 dB bandwidth because, usually, we refer to the normalized quantity $10\log_{10}[P_{diss}(f)/P_{diss}(f_{res})]$: the bandwidth correspond to the frequency interval related to the -3 dB points below the peak. In other words, the dissipations and the external coupling cause the cavity to oscillate in a band of frequencies ($\Delta f|_{3dB} = f_{RF}/Q_L$) whose width is a function of the loaded quality factor.

Let us now consider a cavity powered by a source (klystron) in pulsed mode at a frequency $f_{RF} = f_{res}$. If we suppose that the generator is switched on at time $t = 0$ with a peak power P_{in} we obtain the following expressions for the accelerating voltage, and dissipated and reflected powers [4]

$$V_{acc}(t) = \frac{2\sqrt{\beta}}{(1+\beta)}\left(1 - e^{-\frac{t}{\tau}}\right)\sqrt{RP_{in}} \qquad \xrightarrow{\beta=1} \qquad V_{acc}(t) = \left(1 - e^{-\frac{t}{\tau}}\right)\sqrt{RP_{in}}$$

$$P_{diss}(t) = P_{in}\frac{4\beta}{(1+\beta)^2}\left(1 - e^{-\frac{t}{\tau}}\right)^2 \qquad \xrightarrow{\beta=1} \qquad P_{diss}(t) = P_{in}\left(1 - e^{-\frac{t}{\tau}}\right)^2$$

$$P_{refl}(t) = P_{in}\left[\left(1 - e^{-\frac{t}{\tau}}\right)\frac{2\beta}{(1+\beta)} - 1\right]^2 \qquad \xrightarrow{\beta=1} \qquad P_{refl}(t) = P_{in}e^{-\frac{2t}{\tau}} \tag{12}$$

where we define the filling time $\tau = 2Q_L/\omega_{res}$.
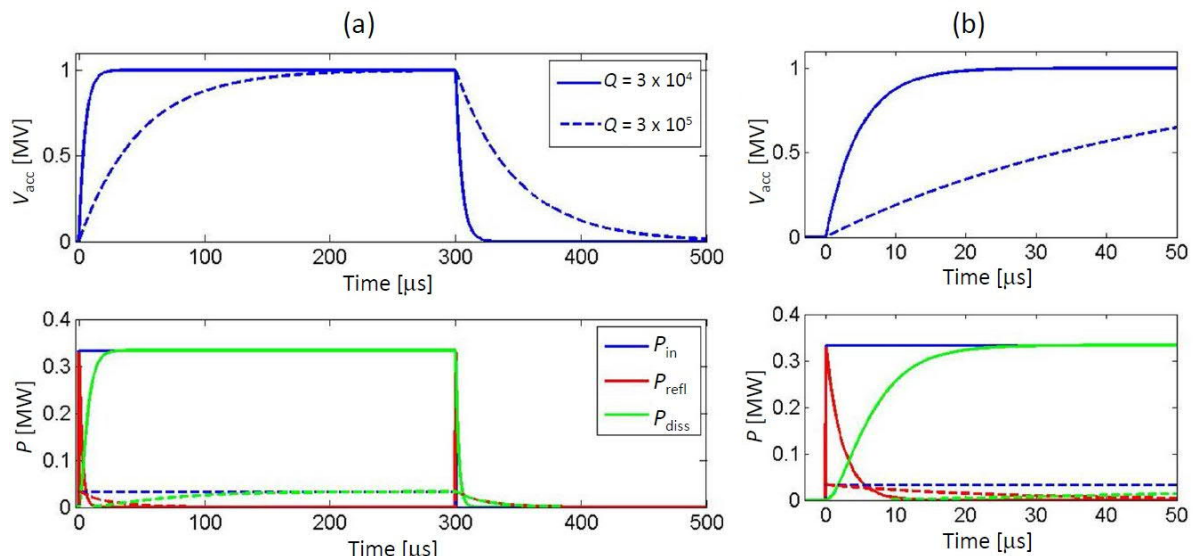
Fig. 6: Accelerating voltage and dissipated and reflected powers as a function of time for two different values of the cavity quality factors, $R/Q = 100$, $\beta = 1$, $f_{res} = 1$ GHz and an accelerating voltage in the regime $V_{acc} = 1$ MV.

The behaviour for a 1 GHz NC cavity with a quality factor $Q_0 = 3 \times 10^4$ is given in Fig. 6, where the accelerating voltage and the dissipated and reflected powers are given as a function of time, assuming $\beta = 1$. In the plot we fixed the accelerating voltage at a regime equal to $V_{acc} = 1$ MV and we have calculated from Eqs. (9) and (12) the needed input power to reach this value. In the same plot we also reported, for reference, a quality factor 3×10^5 that is still, at least, four orders of magnitude lower than the Q-factor of a typical superconducting structure. The plots and the previous formulas clearly show the following important results:

i) The input power we need to reach the desired voltage is inversely proportional to the quality factor of the cavity according to

$$P_{in} = \frac{V_{acc}^2}{\left(\dfrac{R}{Q}\right)} \frac{1}{Q_0} \propto \frac{1}{Q_0} \tag{13}$$

and the dissipated power into the structure follows the same scaling. This means that, as example, to reach a 1 MV accelerating voltage with a NC cavity at 1 GHz we need an input power of the order of a few hundreds of kilowatts, while for a superconducting cell it scales to a few watts.

ii) There is a peak of reflected power back to the generator at the beginning (and at the end) of the input pulse that requires protection for the generator itself to avoid damage.

iii) The voltage in the cavity grows with a filling time proportional to the quality factor of the cavity $\tau = 2Q_L/\omega_{res}$.

Typical filling times for NC cavities are of the order of a microsecond while for a SC cavity they are hundreds of milliseconds. This is also the reason why it is difficult to represent, in the same plot, a NC cavity and an SC one; and we have chosen a value of $Q = 3 \times 10^5$ instead of 10^9 to 10^{10}.

## 2.3 Multi-cell standing wave cavities

In a multi-cell structure, there is one RF input coupler that feeds a system of coupled cavities as sketched in Fig. 1(a). The field of adjacent cells is coupled through the cell irises (and/or through properly designed coupling slots). It is quite easy to demonstrate that the shunt impedance is N times the impedance of a single cavity; moreover, with one source, it is possible to feed a set of cavities with a

simplification of the power distribution system and layout. On the other hand, the fabrication of multi-cell structures is more complicated than single-cell cavities.

The *N*-cell structure behaves like a system of *N* coupled oscillators with *N* coupled multi-cell resonant modes. As an example, the field configuration of a two-cell resonator is shown in Fig. 7. The mode in which the two cells oscillate with the same phase is called 0 mode, while the one with 180° phase shift is called π-mode. It is possible to demonstrate that the most efficient configuration (generally used for acceleration) is the π-mode, which has been shown in Fig. 1(a) for a system of five cells.
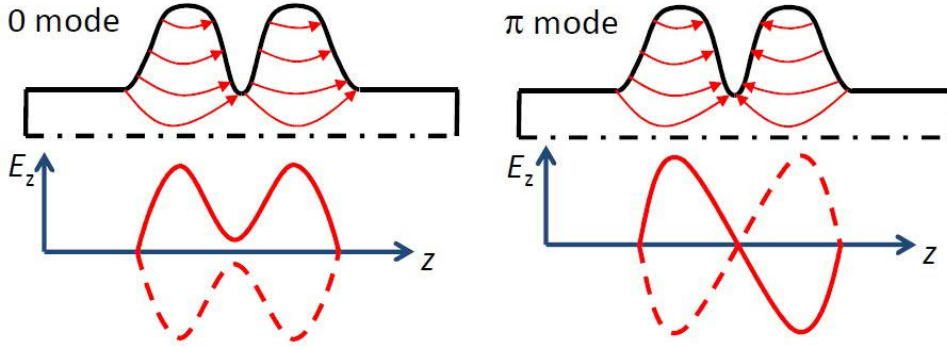
Fig. 7: Resonant mode in a system of two coupled cavities. The mode typically used for acceleration is the π-mode.

In order to have a synchronous acceleration in each cell, the distance (*d*) between the centre of two adjacent cells has to be $d = v/(2f_{RF})$ where *v* is the particle velocity.

Field amplitude variation from cell to cell should be also small, to maximize the acceleration efficiency. This requires a careful realization procedure, which is sometimes not sufficient to reach field flatness below a few percent, and thus requires a tuning process after fabrication.

It is possible to demonstrate that, over a certain number of coupled cavities, the overlap between adjacent modes can introduce problems for field equalization, and this limits the maximum number of multi-cell structures to around 10. It is possible to overcome this limit, for example working in the π/2 mode, but typically these types of structures are not used in FELs or ERLs and their description is beyond the purpose of this paper (further details can be found in the literature, for example in [4]).

For multi-cell structures, it is also useful to introduce another parameter *r*, the shunt impedance per unit length, simply given by

$$r = \frac{R}{L} = \frac{\left(V_{acc}/L\right)^2}{P_{diss}/L} = \frac{E_{acc}^2}{p_{diss}} \qquad \left[\frac{\Omega}{m}\right] \tag{14}$$

where *L* is the total structure length, E_{acc} is the average accelerating field and p_{diss} is the dissipated power per unit length.

As an example, the SC cavities of the European X-FEL operate with modules of nine cells, as sketched in Fig. 8. The parameters of these cavities are given in Table 1. More details can be found in [5, 6].
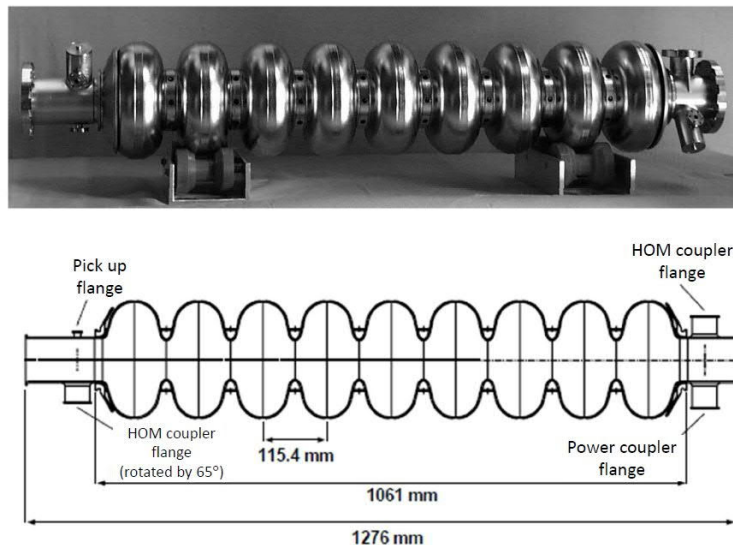
Fig. 8: Multi-cell superconducting cavity of the European X-FEL (courtesy [6])

Table 1: XFel SC cavity parameters

| Parameter	Value
Frequency of operation	1.3 GHz
Mode of operation	π
R/Q	1036 [Ω]
Q_0	10^{10}
Q_L	4.6×10^6
Number of cells	9
Active length	1.038 [m]
Accelerating gradient	23.6 [MV/m]
RF pulse length	1.4 [ms]
Repetition rate	10 [Hz]
Iris diameter	70 [mm]
E_{peak}/E_{acc}	2
B_{peak}/E_{acc}	4.26 [mT/(MV/m)]

2.4 Beam structure

The discussion so far allows a better understanding of the relation between the beam structure and the type of accelerating sections. RF structures are, in general, fed by pulses, and each pulse includes several RF periods as reported in Fig. 9(a). As already remarked, the duty cycle is defined as the ratio between the pulse width and the period. The corresponding accelerating voltage in the cavity is sketched in Fig. 9(b). To avoid energy modulation along the bunch train, the electrons can be accelerated only in the flat part of the voltage pulse (in the case of high beam currents, injection during the voltage slope, or RF gymnastics, is also possible to compensate for the so-called beam loading effects, but the discussion of these techniques is beyond the scope of the present paper).

From consideration of the paragraphs above, it is straightforward to see that high DC operation (up to CW operation) is feasible only with SC structures, while low DC operation (DC $< 10^{-3}$) is also feasible with NC structures. The reasons are clearly due to the power available from RF sources, power dissipation and filling times of the structures. In the case of SC, in fact, long RF pulses are required to fill the cavities (the higher the quality factor, the higher the filling time), but relatively low average power is required from the RF source to reach a given gradient, since a small amount of power is dissipated into the structures. In the second case, instead, short RF pulses (~µs) with high peak power

are used but, in order to limit the average power required from the RF generator and dissipated into the structure, the overall DC has to be kept small. This implies that the maximum number of pulses per second has to be lower than a few hundred.

From what has been highlighted in the paragraphs above it follows that multi bunch operation (from hundreds of bunches up to CW) is preferred with SC structures, because of the long pulses used.
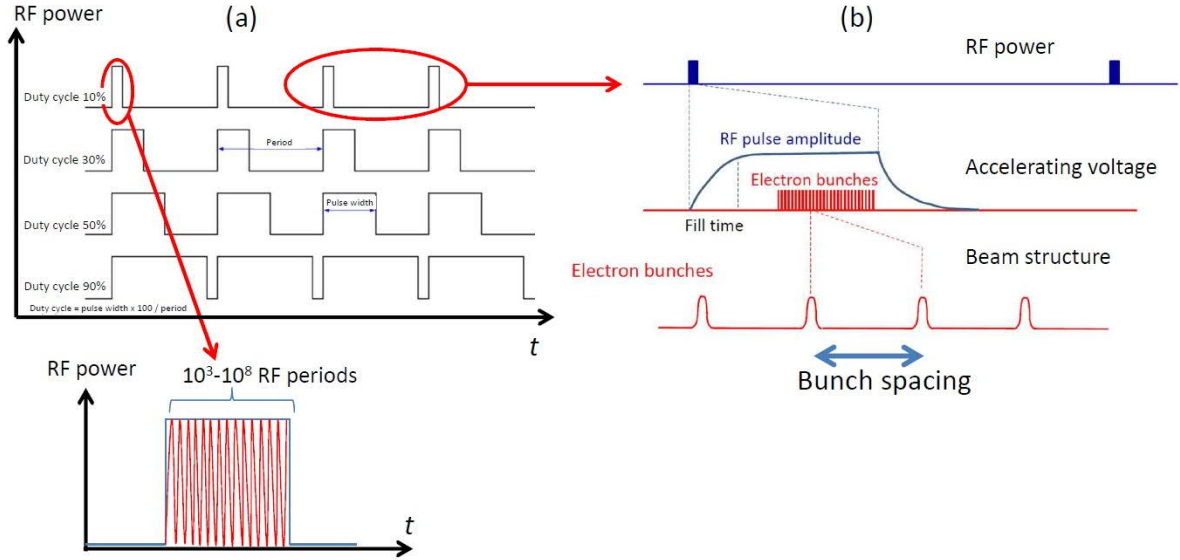
Fig. 9: (a) Sketch of the input power into RF structures and (b) related beam structure

3 Travelling wave structures

As pointed out in the first paragraph, there is another possibility for accelerating particles: using a travelling wave (TW) section. The RF wave is co-propagating with the beam with a phase velocity equal to the beam velocity (*c*).

In other words, a TW structure is a special waveguide in which the phase velocity of the wave matches the particle velocity. Only in this case, the beam can efficiently absorb energy from the EM wave, and results in continuous acceleration. The solutions of Maxwell's equations for an EM wave propagating into a constant cross-section waveguide, however, give a phase velocity that is always larger than the speed of light. Thus, such an EM wave will never be synchronous with a particle beam. For instance, if we consider a circular waveguide (Fig. 10(a)), it turns out that the first propagating mode with $E_z \neq 0$ is the TM_{01} mode whose longitudinal electric field can be expressed by the well know formula [7]

$$E_z\big|_{TM_{01}} = E_0 J_0\left(\frac{p_{01}}{a} r\right) \cos\left(\omega_{RF} t - k_z^* z\right) \tag{15}$$

where *a* is the radius of the waveguide and k_z^* is the propagation constant given by

$$k_z^* = \frac{1}{c}\sqrt{\omega_{RF}^2 - \omega_{cut}^2} \tag{16}$$

where ω_{cut} cut-off angular frequency of the waveguide equal to $\omega_{cut} = c p_{01}/a$.

The corresponding phase velocity is given by

$$v_{\text{ph}} = \frac{\omega_{\text{RF}}}{k_z^*} = \frac{c}{\sqrt{1 - \omega_{\text{cut}}^2 / \omega_{\text{RF}}^2}} \tag{17}$$

which is always larger than c.

The behaviour of the propagation constant as a function of frequency is the well-known dispersion curve, and is sketched in Fig. 10(a). It is important to remark that the phase velocity is not the velocity of the energy propagation into the structure, which, instead, is given by the group velocity (v_g):

$$v_{\text{g}} = \left. \frac{d\omega}{dk_z} \right|_{\omega = \omega_{RF}} = c\sqrt{1 - \omega_{\text{cut}}^2 / \omega_{\text{RF}}^2} \tag{18}$$

and is always smaller than c.
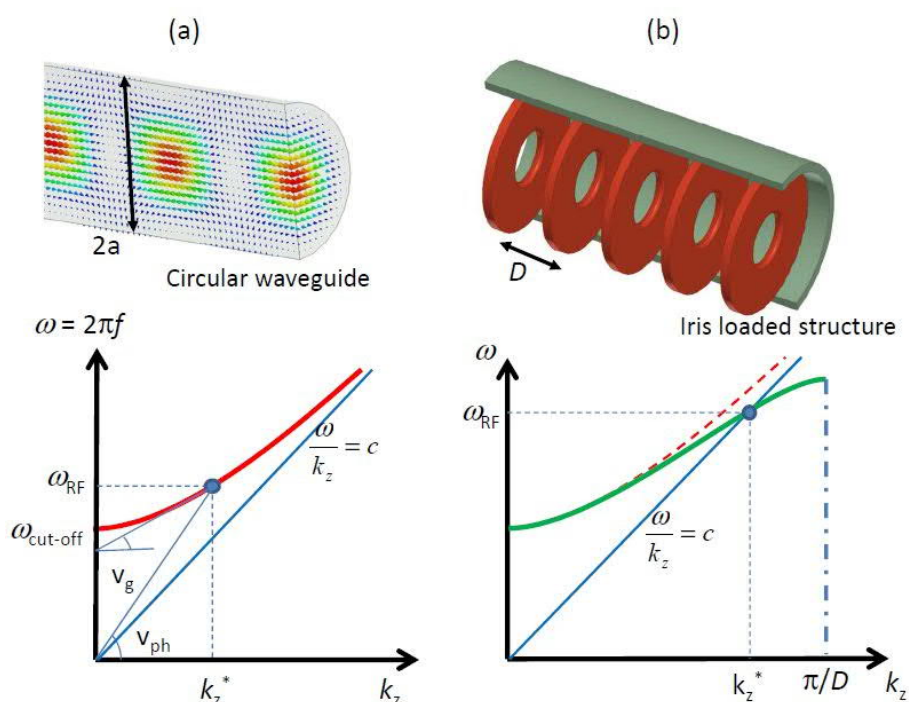
Fig. 10: Typical dispersion curve for (a) a circular waveguide and (b) an iris-loaded structure

In order to slow down the wave phase velocity, the structure through which the wave is travelling is periodically loaded with irises. A sketch of an iris-loaded structure is given in Fig 10(b). The field in this type of structure is that of a special wave travelling within a spatial periodic profile (TM$_{01}$-like mode). The structure can be designed to have the phase velocity equal to the speed of the particles: this allows a net acceleration over large distances.

In particular, the accelerating field can be expressed by Floquet's theorem [4, 7]

$$E_z \big|_{TM_{01-\text{like}}} = \underbrace{E_P(r,z)}_{\substack{\text{periodic function} \\ \text{with period D}}} \cos\left(\omega_{\text{RF}}t - k_z^* z\right) \tag{19}$$

The dispersion curve for this type of structure is given in Fig. 10(b) and shows that, at a given frequency, the phase velocity can be equal to (or even slower than) c.

In a TW structure, the RF power enters into the cavity through an input coupler and flows (travels) through the cavity in the same beam direction; and an output coupler, at the end of the structure, connected to a matched power load, absorbs the non-dissipated power avoiding reflections, as sketched in Fig. 1(b). If there is no beam, the input power simply dissipates on the cavity walls and the remainder is finally dissipated into the power load. In the presence of a beam current a fraction of this power is, indeed, transferred to the beam.
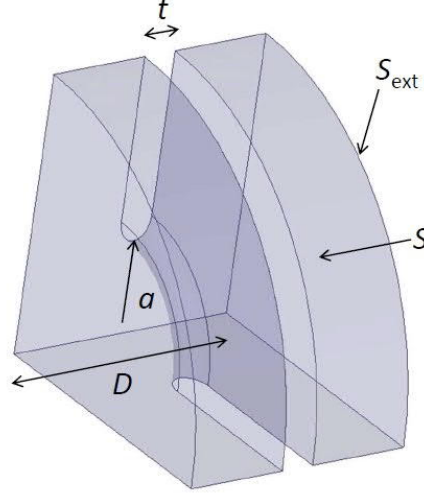
Fig. 11: Sketch of a single cell of a TW structure

3.1 Travelling wave structure parameters

Similarly to what has been done for SW cavities, it is possible to define some figures of merit of TW structures as well. Referring to the single cell sketched in Fig. 11, we can consider the following quantities:

$$V_z = \left| \int_0^D E_z \cdot e^{j\omega_{RF}\frac{z}{c}} dz \right| \qquad \text{single cell accelerating voltage } [V]$$

$$E_{acc} = \frac{V_z}{D} \qquad \text{average accelerating field in the cell } [\frac{V}{m}]$$

$$P_{in} = \int_{Section} \frac{1}{2} \text{Re}\left(\vec{E} \times \vec{H}^* \right) \cdot \hat{z} dS \qquad \text{average input power (power flux) } [W]$$

$$P_{diss} = \frac{1}{2} R_s \int_{\substack{cavity \\ wall}} |H_{tan}|^2 dS \qquad \text{average dissipated power in the cell } [W]$$

$$p_{diss} = \frac{P_{diss}}{D} \qquad \text{average dissipated power per unit length } [\frac{W}{m}]$$

$$W = \int_{\substack{cavity \\ volume}} \overbrace{\left(\frac{1}{4}\varepsilon|\vec{E}|^2 + \frac{1}{4}\mu|\vec{H}|^2 \right)}^{energy\,density} dV \qquad \text{stored energy in the cell } [J]$$

$$w = \frac{W}{D} \qquad \text{average stored energy per unit length } [\frac{J}{m}]$$

(20)

The shunt impedance per unit length r is defined in Eq. (14) as

$$r = \frac{E_{acc}^2}{p_{diss}} \qquad \left[\frac{\Omega}{m} \right]$$

The higher the value of *r*, the higher the available accelerating field for a given RF power. Typical values for a 3 GHz structure are ~60 MΩ/m.

In a purely periodic structure, made by a sequence of identical cells (also called a 'constant impedance structure'), the RF power flux and the intensity of the accelerating field decay exponentially along the structure. The process of power filling is represented in Fig. 12. When the RF generator is switched on, the power starts flowing into the structure with a velocity equal to the group velocity, which is typically a small fraction of the velocity of light (a few percent). The time necessary to propagate the RF wavefront from the input coupler to the end of a section of length *L*, referred to as the filling time, is given by

$$\tau_F = \frac{L}{v_g} \quad [s] \tag{21}$$

where the group velocity can be calculated by

$$v_g = \frac{P_{in}}{w} \quad \left[\frac{m}{s}\right] \tag{22}$$
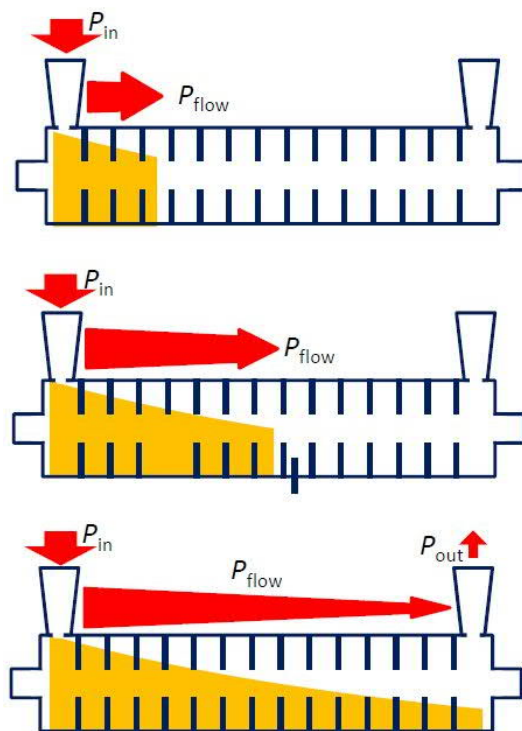
Fig. 12: Sketch of the power filling of a TW structure

After one filling time the structure is completely full of energy.

Increasing the group velocity allows reduction of the duration of the RF pulse powering the structure. Since $w \propto E^2$, however, a low group velocity is preferable to increase the effective accelerating field for a given power flowing in the structure. It is possible to demonstrate that the group velocity scales as a^3 where *a* is the iris's aperture.

Due to the power attenuation along the structure, after one filling time the accelerating field can be expressed as

$$E_z\big|_{TM_{01-like}} = E_P(r,z)\cos\left(\omega_{RF}t - k_z^* z\right)e^{-\alpha z} \tag{23}$$

where the attenuation constant is given by

$$\alpha = \frac{p_{\text{diss}}}{2P_{\text{in}}} \quad \left[\frac{1}{\text{m}}\right] \tag{24}$$

The field sampled by a particle entering the structure after one filling time is simply given by

$$E_z(z) = E_P(z) e^{-\alpha z} \tag{25}$$

Due to the periodicity of the structure, this field has an amplitude modulation with period D (in the term $E_P(z)$). Also, for TW structures it is possible to define the quality factor

$$Q = \omega_{\text{RF}} \frac{w}{p_{\text{diss}}} \tag{26}$$

which can, from Eqs. (22) and (24), be related to the attenuation constant α

$$Q = \frac{\omega_{\text{RF}}}{2v_{\text{g}}\alpha} \tag{27}$$

Each structure is identified by a field phase advance per cell given by: $\Delta\varphi = k_z^* D$. For several reasons well-illustrated in [8], one of the most common modes used for acceleration is $2\pi/3$.

As an example, we can consider a 2 m long C-band ($f_{\text{RF}} = 5.712$ GHz) accelerating section made of copper. Using an iris aperture $2a = 14$ mm, we obtain for the $2\pi/3$ mode typical values of the abovementioned parameters: $r = 82$ [MΩ/m], $\alpha = 0.36$ [1/m], $v_g/c = 1.7\%$. This gives a filling time $\tau_F = 150$ ns, which is much lower than typical values obtainable with SW structures working at the same frequency. In Fig. 13(a) is shown the power flow along the structure, and the corresponding accelerating field, assuming a pulsed input power of 50 MW. The power dissipated into the structure and the total accelerating voltage integrated by a particle entering into the section at different times are shown in Fig. 13(b). From the figure, it is possible to observe that after one filling time the structure is full of energy, and the integrated voltage sampled by a particle does not change.
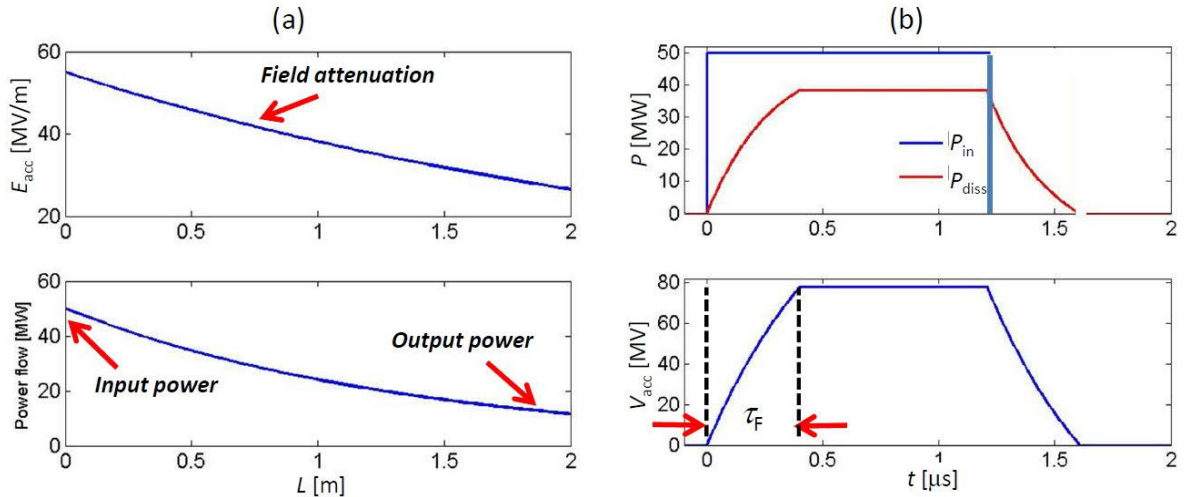
Fig. 13: (a) Accelerating field and power flow; (b) input power, cavity dissipated power and accelerating voltage, for a C-band constant impedance structure working on the $2\pi/3$ mode.

At the end of the structure, the remaining power has to be dissipated into an external load to avoid reflections. These, in fact, can travel back to the RF power unit (causing possible damage), locally increase the peak fields (causing possible discharges) or can produce undesirable perturbations to the beam dynamics.

Typically, TW structures have very short filling time values (<1 μs) and allow operation in pulsed mode at low repetition rate (10 Hz to 100 Hz) with high peak power (tens of MW) and relatively high accelerating field (up to 50 MV/m). Typical DC are very low (10^{-4} to 10^{-5}). For instance, assuming the previously mentioned TW structure being fed by 400 ns RF pulses of 50 MW (P_{in}) at 100 Hz, the resulting DC is 4×10^{-5} with a total average power from the RF generator of 2 kW ($P_{in} \times$ DC). The use of short RF pulses, however, gives the possibility of accelerating just a few bunches per RF bucket.

In conclusion, note the following important remarks.

i) Due to the power dissipation and the consequent reduction of the accelerating field, increasing the TW cavity length too much makes the acceleration process very inefficient. Typically in the S-band (3 GHz) the cavity length is limited to 3 m, in the C-band (6 GHz) to 2 m.

ii) There is no benefit preferring SC materials for TW structure fabrication. This is a direct consequence of the TW working principle, where there is no accelerating field build-up effect limited by ohmic losses, and thus the obtainable gain using SC materials is not relevant. It would be, theoretically, only using a very long TW structure, but this would imply very long RF pulses at high peak voltage (not feasible) together with a dramatic complication of the realization process.

iii) Since the structure is basically a waveguide with irises, at the input port there are no significant power reflections towards the generator, and thus it is possible to connect the power unit directly to the section without circulators/isolators to protect the source.

3.2 Travelling wave constant gradient structures

An example of constant impedance TW structures has been presented in the previous section. Irises of equal dimensions cause the accelerating field to decay exponentially along the section. It is possible to demonstrate that, in order to keep the accelerating field constant in the whole structure, the iris aperture has to be correctly shrunk along the structure [4, 8]. In this way, the field attenuation is compensated for by the increase of the stored energy per unit length, due to the lower group velocity. For instance, in Fig. 14 the iris dimensions and the section parameters for a 100-cell C-band constant gradient and constant impedance structure have been reported as a function of the cell number. In both cases the average accelerating field is the same and equal to 40 MV/m for 50 MW input power. Because of the different iris dimensions, the group velocity and shunt impedance also change along the structure.

In general, constant gradient structures are more efficient than constant impedance structures, because of the more uniform distribution of RF power in the longitudinal direction, but they require a more complicated mechanical realization due to the irises' profile modulation.

As a reference, the parameters of the TW accelerating structures of the SLAC linac [8] (used for the LCLS FEL), the PSI SwissFEL [9–12] and Spring 8 XFEL linac [13, 14] are reported in Table 2. The former operates in the S-band, while the others are in the C-band.
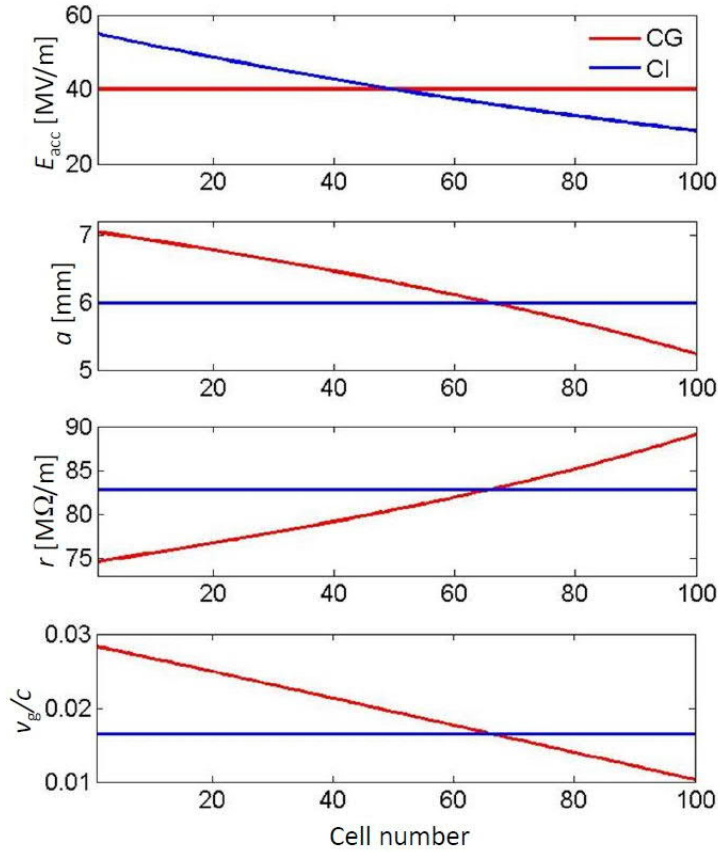
Fig. 14: Iris dimensions and structure parameters for 100-cell C-band constant gradient (red line) and constant impedance (blue line) structures.

Table 2: Parameters of the TW structures of the SLAC linac [8] (used for the LCLS FEL), PSI SwissFEL [9–12] and Spring 8 linacs [13, 14].

Parameter	LCLS TW structures	PSI SwissFEL structures	Spring 8
Operating frequency [GHz]	2.856	5.712	5.712
Operating mode	$2\pi/3$	$2\pi/3$	$3\pi/4$
Structure length [m]	3	2	1.8
Type of structures	CG	CG	Quasi-CG, damped
Number of cells	86	113	91
Accelerating gradient [MV/m]	22	28	38
Filling time [µs]	0.83	0.32	0.3
Cell iris diameter [mm]	26.2 to 19.1	14.4 to 10.9	13.6 to 17.3
Shunt impedance [MΩ/m]	53 to 60	74 to 88	49 to 59
Group velocity [v_g/c]	2.04% to 0.65%	3.08% to 1.21%	2% (av.)
Repetition rate [Hz]	120	100	10 to 60

4   Materials for accelerating structure fabrication

In the previous sections the main characteristics of the accelerating structures with their main figures of merit, properties and geometries have been illustrated. We will now go into the details of linac technology, starting with the material generally used for the structure's realization. As already pointed out the most common alternatives are oxygen-free high conductivity (OFHC) copper for NC cavities, and niobium for the SC ones.

4.1 Oxygen-free high conductivity copper

OFHC copper is the most common material used for NC structures for several reasons:

i) it has a very good electrical (and thermal) conductivity;

ii) it has a low Secondary Emission Yield (SEY) that allows the avoidance of multiple impact electron amplification (multipacting) phenomena [15] during structure power up, conditioning and operation;

iii) it shows good performance at a high accelerating gradient;

iv) it is easy to machine, and a very good roughness (up to the level of a few nm) can be achieved;

v) it can be brazed or welded.

The microwave surface resistance of the copper (as for all metals) is expressed by

$$R_s = \sqrt{\frac{\pi f_{RF}\mu_0}{\sigma}} = \frac{1}{\sigma\delta} \tag{28}$$

where σ is the conductivity ($\sim5.8 \times 10^7$ S/m for Cu at 20°C) and δ is the skin depth, which represents the penetration of the EM field and surface currents inside the metal, as sketched in Fig. 15(a), given by

$$\delta = \frac{1}{\sqrt{\pi f_{RF}\mu_0\sigma}} \tag{29}$$

The behaviour of the surface resistance and skin depth as a function of frequency is shown in Fig. 15(b). The conductivity increases reducing the temperature. In the DC regime, for instance, it can be more than a factor of 100 higher (depending on the copper purity) at cryogenic temperatures with respect to room temperature. At cryogenic temperatures (<40 K) and in the RF regime, however, a mechanism called the 'anomalous skin effect' [16] takes place. This reduces the gain to a factor of about 20 (depending on the working frequency and copper purity). This also translates into a reduction of the gain in the quality factor, which makes the use of copper at cryogenic temperatures neither practical nor convenient.
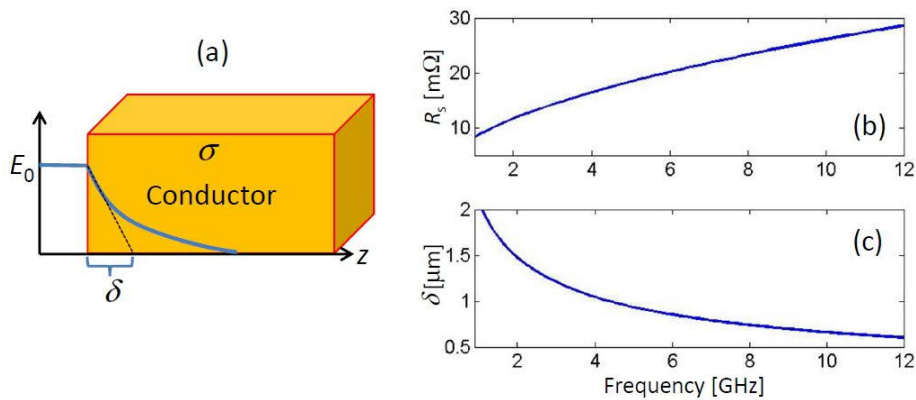
Fig. 15: (a) Sketch of the penetration of RF EM fields and surface currents inside metal; behaviour of (b) copper surface resistance and (c) skin depth as a function of frequency.

4.2 Niobium

Superconductivity was discovered in 1911. For a SC material below its critical temperature T_c, in the DC regime, resistance is zero. In the RF regime, however, the surface resistance is always larger than zero (even if orders of magnitude lower than NC materials), because not all the electrons are in the superconducting state. The residual ones are not completely shielded by the superconducting currents

and thus experience a residual electric field, dissipating power. At frequencies below 10 GHz (and temperatures below $T_c/2$), the experimental data available for several materials are well described by the empirical relation [17–21]

$$R_s = \underbrace{A\frac{\omega_{RF}^2}{T}e^{-\alpha\frac{T_c}{T}}}_{R_{BCS}} + R_{res} \tag{30}$$

The first term, resistance (R_{BCS}), is well explained by a theoretical model of the superconductor. In this term the coefficients A and α depend on the material. The second term is a residual term due to impurities in the material.

The SC state can be destroyed by an external magnetic field larger than a critical field H_c that depends on the material used. In practice, this effect fixes the maximum theoretical field that a SC cavity can sustain.

The most common material for the fabrication of SC cavities is niobium for several reasons [21–23]:

i)   it has a relatively high transition temperature ($T_c = 9.25$ K);

ii) it has a relatively high critical magnetic field, $H_c = 170$ mT to 180 mT;

iii) it is chemically inert;

iv) it can be machined and deep drawn;

v)   it is available either as bulk or sheet in any size, fabricated by forging and rolling;

vi) large grain sizes (often favoured) can be obtained by e-beam melting;

vii) it can also be used as a coating (e.g. by sputtering) on NC materials like Cu;

viii) it has good thermal stability and is of relatively low cost.

The R_{BCS} resistance for Nb is given by

$$R_{BCS} = 2\times10^{-4}\frac{\left(f_{RF}[\text{MHz}]/1500\right)^2}{T}e^{-\frac{17.67_c}{T}} \quad [\Omega] \tag{31}$$

while the residual resistance can vary between 5 nΩ and 20 nΩ.

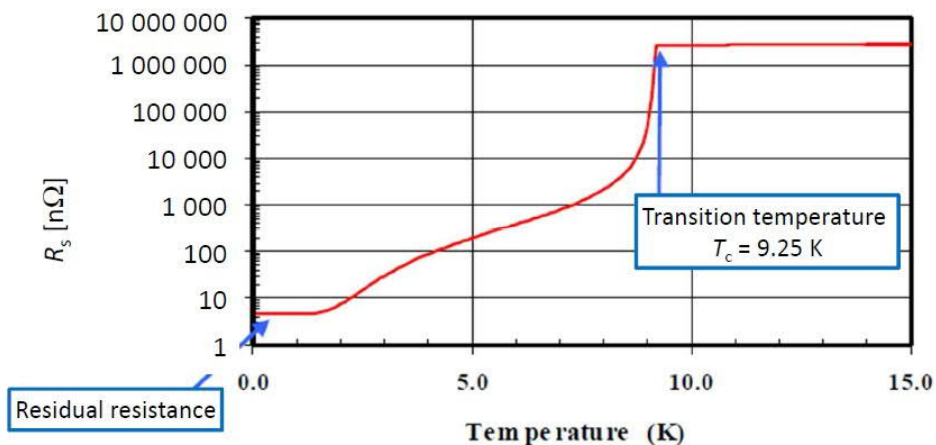The behaviour of niobium resistance as a function of temperature at 700 MHz is shown in Fig. 16.

Fig. 16: Surface resistance of Nb at 700 MHz (courtesy [19])

5   Cavity parameters' scaling with frequency

The material properties, described in the previous section, allow understanding the frequency scaling laws of cavity parameters, which have been summarized in Table 3. For the sake of completeness, in the bottom rows of the table the scaling of the wakefield intensities have also been reported. These have an important impact on beam dynamics, and their description is beyond the scope of this paper. For our purposes, it is only important to remark that, the higher the wakefield intensity, the higher is the possible perturbation in single-bunch and multi-bunch beam dynamics.

Table 3: Scaling laws for cavity parameters with frequency

Parameter	NC	SC
Surface resistance (R_s)	$\propto f^{1/2}$	$\propto f^2$
Quality factor (Q)	$\propto f^{-1/2}$	$\propto f^{-2}$
Shunt impedance per unit length (r)	$\propto f^{1/2}$	$\propto f^{-1}$
r/Q	$\propto f$	
Longitudinal wakefield ($w_{//}$)	$\propto f^2$	
Transverse wakefield ($w_\perp$)	$\propto f^3$	

r/Q increases at high frequency. For NC structures, r also increases and this push to adopt higher frequencies. For SC structures, since the power losses increases with f^2, r scales with $1/f$ and this push to adopt, in principle, lower frequencies. On the other hand, at higher frequencies the beam–cavity interaction due to wakefields becomes more critical ($w_z \propto f^2$, $w_\perp \propto f^3$) and commercial power sources (above 6 GHz) are less commonly available. Cavity fabrication at very high frequency requires higher precision and critical alignment but, on the other hand, at very low frequencies one needs more material and larger machines for the fabrication of components.

These points clearly show that a compromise is required, and for conventional FEL and ERL this basically fixes the operational frequency for SW SC cavities between 500 MHz and 1500 MHz, for TW NC structures between 3 GHz and 6 GHz and for SW NC structures between 0.5 GHz and 3 GHz.
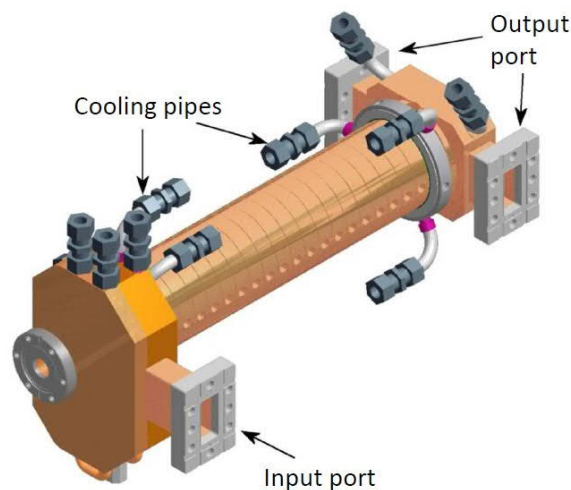

Fig. 17: Mechanical drawing of a small prototype of a C-band TW structure with a reduced number of accelerating cells.

6   Linac technology issues for normally conducting travelling wave structures

TW NC structures are usually a few metres long. They are made of hundreds of cells, and an input and an output coupler (the latter connected to an RF load). As an example, the mechanical drawing of a

small prototype of a C-band TW structure with a few accelerating cells is given in Fig. 17. As has already been pointed out, these structures typically operate with short RF pulses (between 0.5 μs and 1.5 μs) in a single bunch or with a few bunches, with high peak power RF pulses (~50 MW). The accelerating field inside such structures is relatively high (ranging from 20 MV/m to 50 MV/m), and the mode of operation is, generally, the $2\pi/3$ mode. The typical frequency bands of operation are S or C (3 GHz and 6 GHz, respectively). TW cells' geometries and, in particular, the irises' dimensions and profiles are optimized to reach a good compromise between a high shunt impedance (which favours small irises) and a short filling time (which favours large irises). As an example, Fig. 18 shows the cell parameters as a function of the iris dimensions for a C-band structure. Peak surface electric fields occur on the irises separating adjacent cells, as shown in Fig. 19(a), where we report the magnitude of the electric field in a C-band accelerating cell with 30 MV/m average accelerating field. Peak field values are typically a factor of 2–2.5 larger than the accelerating one. The magnetic field distribution, for the same average accelerating field, is given in Fig. 19(b). It occurs on the outer walls of the cells (as for TM_{01} mode). Cooling pipes are inserted or brazed around the cells to guarantee temperature stability of the structures, thus avoiding detuning under high power feeding, as shown in Fig. 24(c) below, where we report pictures of a fabricated cell.
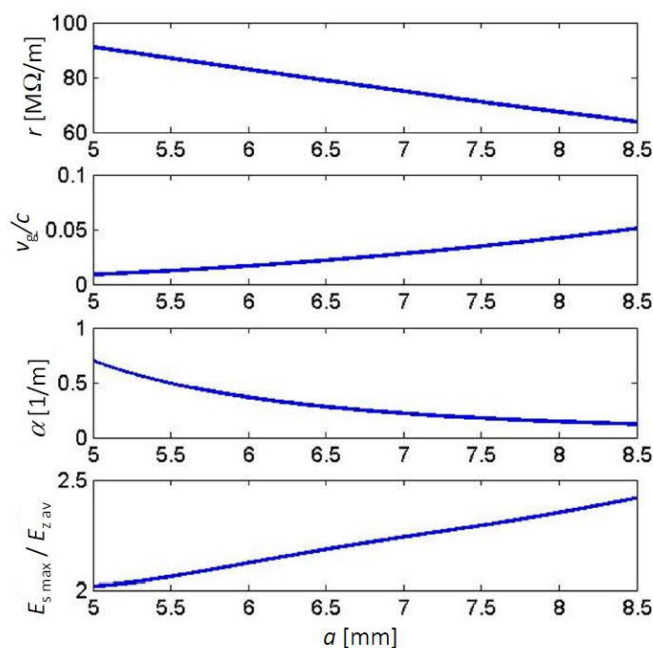

Fig. 18: Cell parameter as a function of the iris dimensions for a C-band structure
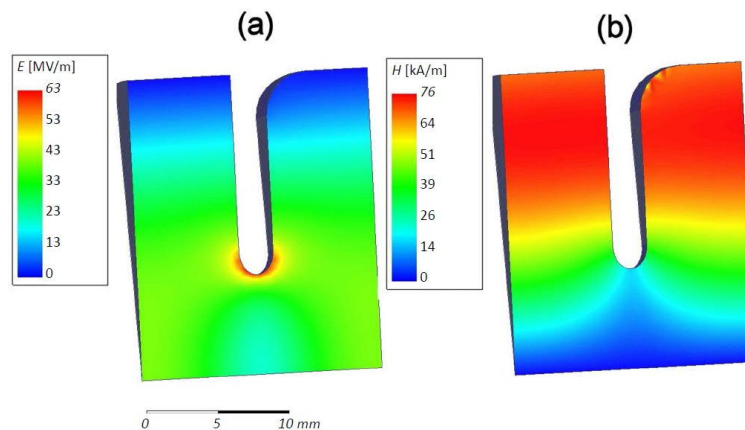
Fig. 19: (a) Electric field and (b) magnetic field intensity for a C-band accelerating cell with 30 MV/m average accelerating field on the axis.

The structures are fed by waveguides coupled by means of slots in a so-called 'coupling cell' that matches the TE_{10} mode of the waveguide with the travelling wave mode (TM_{01}-like), as shown in Fig. 20 [3, 24]. Either J-type couplers [13], or couplers with integrated splitters, allow a symmetric feed that compensates for the dipole kicks in the coupling cell, which are present if there is only a single slot, as shown in Fig. 21. In the coupling slot between the waveguides and the cavity we can have a high magnetic field and, as a consequence, high pulsed heating that can increase breakdown phenomena [3]. For this reason, rounded shapes are frequently used (as sketched in Fig. 22). Moreover, racetrack profiles allow for compensation of the quadrupole distortions of the field in the coupling cells introduced by the coupling holes for the waveguides. The typical magnitude and phase of the accelerating field in a short C-band TW structure are plotted, as an example, in Fig. 23. In the plot we can recognize the $2\pi/3$ phase advance from cell to cell and the periodic profile of the accelerating field (where the maximum field occurs in the centre of each cell).
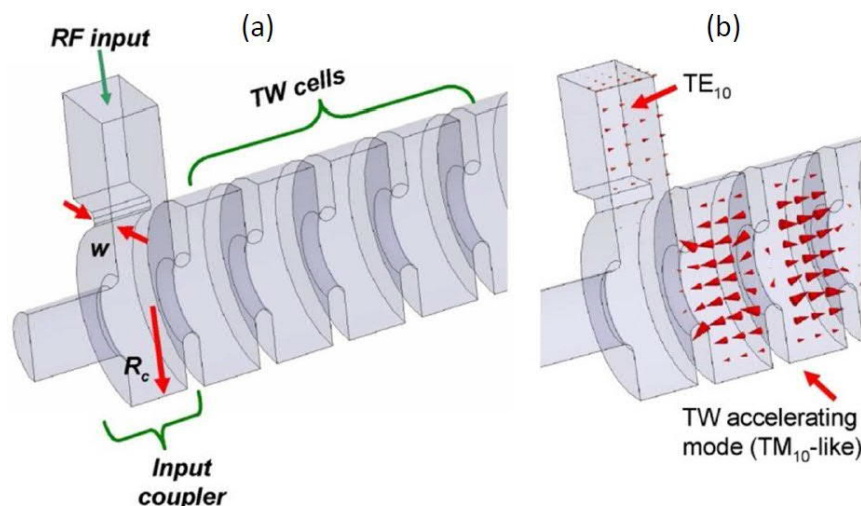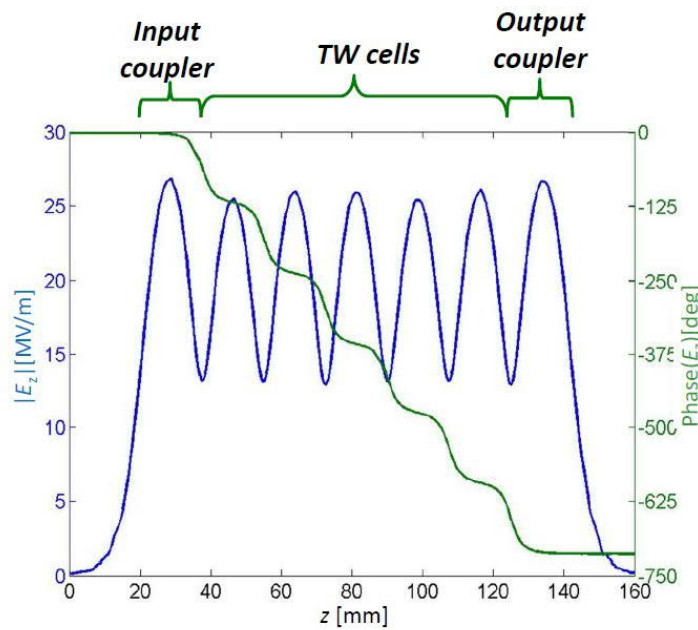

Fig. 20: (a) Coupling of the waveguide network to a TW structure; (b) in the input coupler the TE_{10} mode of the waveguide is matched to the travelling wave mode (TM_{01}-like).
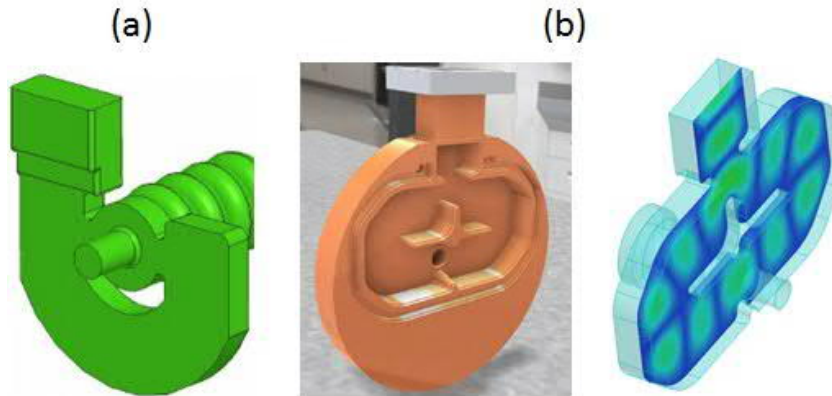
Fig. 21: Example of couplers with symmetric feeding to avoid dipole kicks: (a) J-type couplers (b) couplers with splitters.
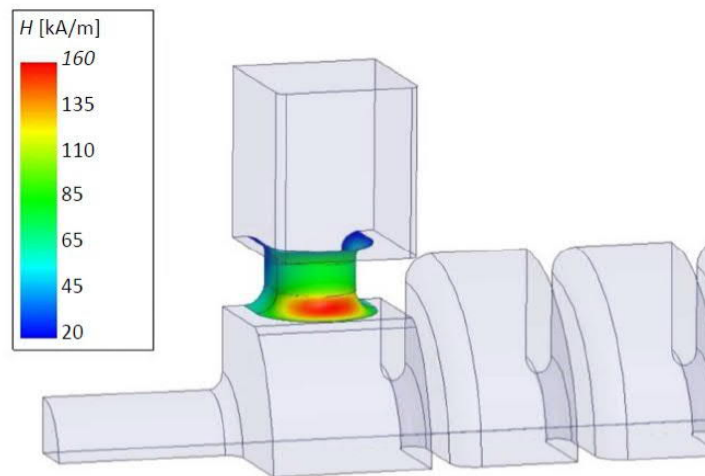

Fig. 22: Magnetic field in the coupler region

Fig. 23: Accelerating field in magnitude (blue) and phase (green) in a short C-band TW structure with 20 MV/m average accelerating field.

The whole fabrication process sequence is reported in Fig. 24. Cells and couplers are typically realized starting from OFHC forged or laminated copper (Fig. 24(a)) using milling machines and lathes (Fig. 24 (b)), with a precision that can be of the order of a few micrometres and a surface roughness that can reach values below 50 nm. The cells are then cleaned, piled up (Fig. 24(c) and (d)) and brazed together in vacuum or hydrogen furnaces (Fig. 24(e)), using different alloys at different temperatures (700°C to 1000°C).
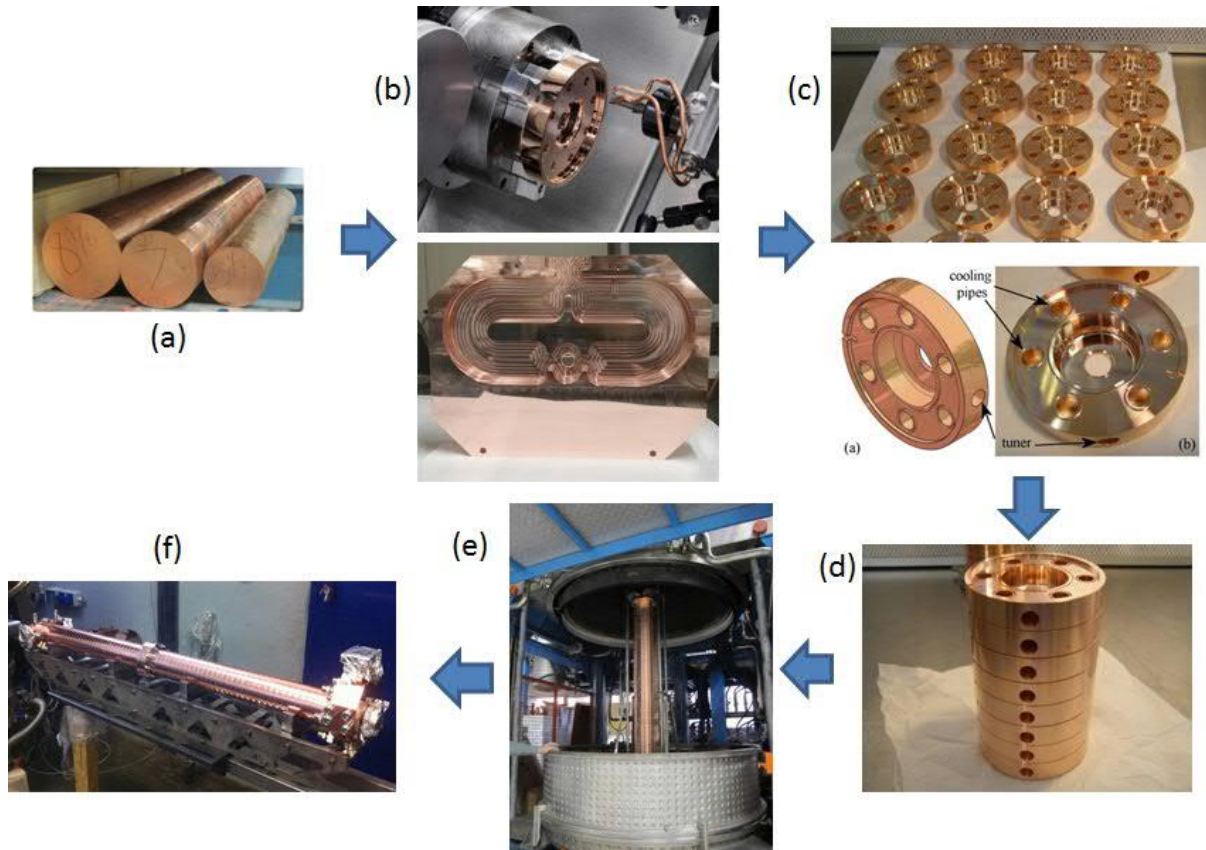
Fig. 24: Sequence of the fabrication process of a TW structure: (a) OFHC forged copper; (b) realization of cells by lathes; (c) single cells machined and ready to be stacked; (d) cells piled up before brazing; (e) the structure in a vacuum or hydrogen furnace; (f) the brazed structure.

To compensate for deformations and imperfections that can occur during the brazing process, tuning of TW structures is often necessary. The standard method is to measure the field inside the structure using a perturbation technique (the Steele method [25]), and adjusting the phase advance per cell to the correct value by deforming the outer volume of the cells with 'deformation tuners'. A structure during a tuning procedure is shown in Fig. 25, while Fig. 26(a) represents the section of one cell, where deformation tuners have been designed to reduce the thickness of the walls in three points, and allow plastic deformations of the internal surface (shown in Fig. 26(b)). An example of the measured field before and after a tuning procedure is given in Fig. 27 for a 70-cell C-band structure [26]. The same plot also reports the relative phase advance per cell. Tuning algorithms must be used to calculate from the complex field measurements the deformation to be applied to the cells [27]. The final goal of a cell-to-cell phase error is typically ±2°, with a cumulative phase advance in the overall structure within ±5° [28].
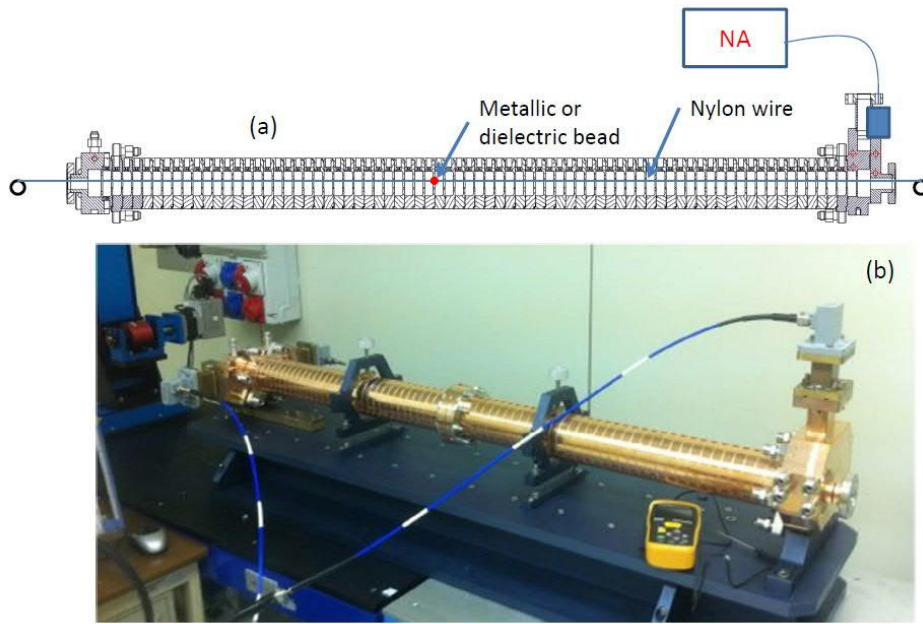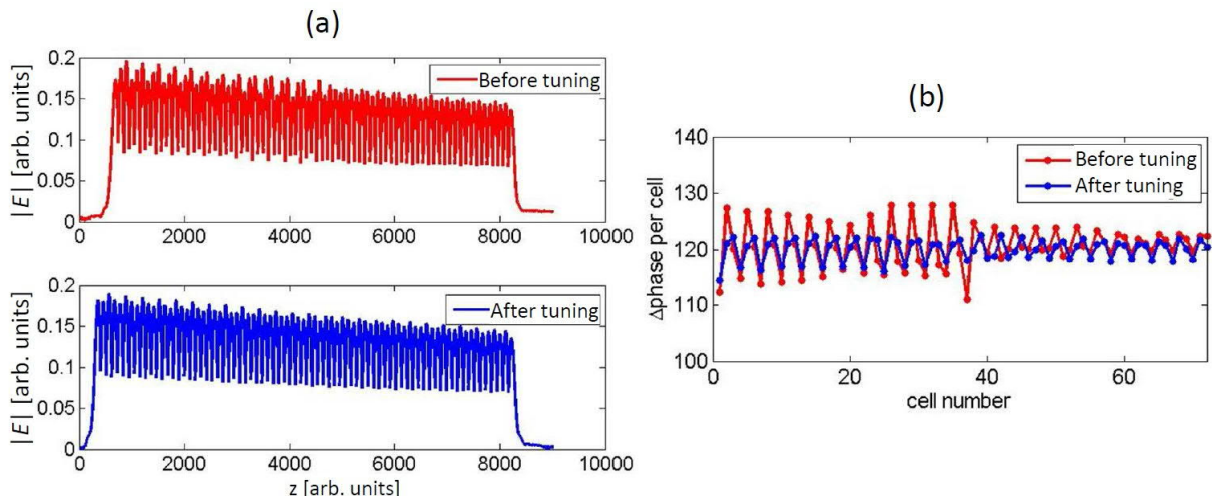
Fig. 25: TW structure during low-power RF measurements and tuning: (a) schematic layout; (b) picture of the cavity.
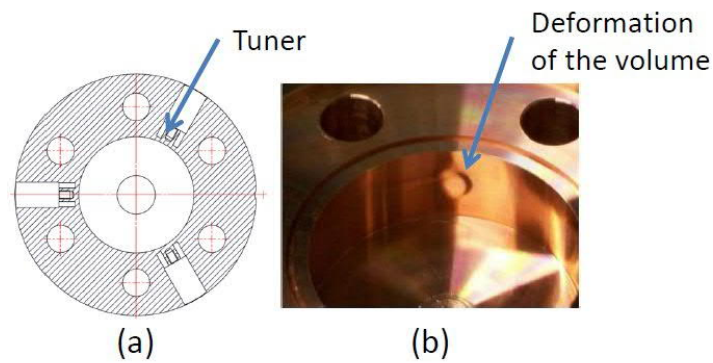
Fig. 26: (a) Section of one cell with deformation tuners reducing the thickness of the walls at three points; (b) deformation of the internal surface after tuning.

Fig. 27: (a) Measured accelerating field before and after the tuning procedure; (b) phase advance per cell before and after tuning.

TW structures require pulsed sources with a high peak power. For this purpose, klystron and RF compression systems (SLAC Energy Doubler, SLED) are usually adopted. As an example, we report in Fig. 28 a schematic of the RF network of the XFEL at Spring 8 [13]. The TW structures are quasi-constant gradient, working in the C-band with $3/4\pi$ phase advance. Their main parameters are reported in Table 2 [13]. They are fed by klystrons whose 2.5 μs RF pulse is compressed down to 0.5 μs with the use of SLED-type (SLED-SLAC Energy Doubler) cavities. In this way, an accelerating field of 38 MV/m can be reached.
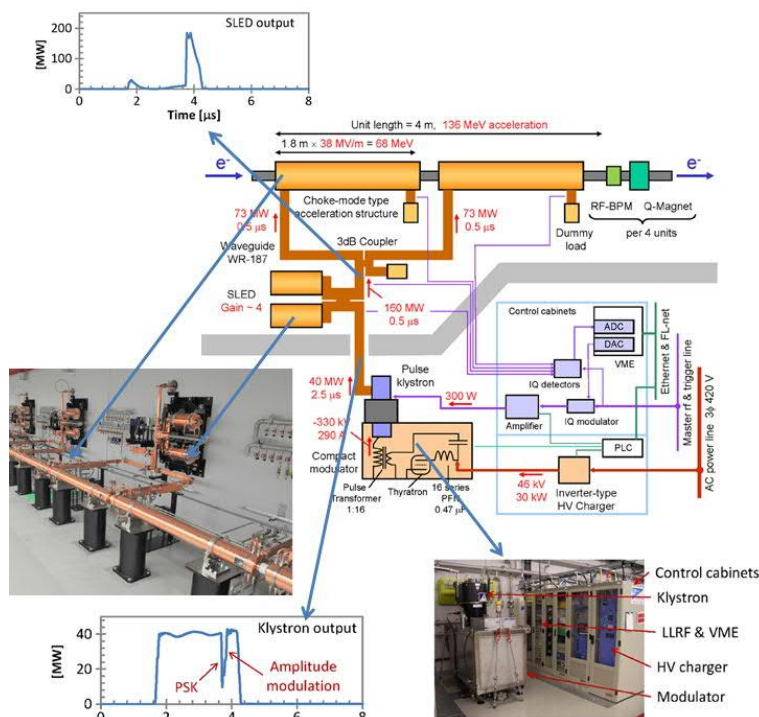
**Fig. 28:** Schematic of the RF network of the XFEL at Spring 8 (courtesy [13, 14])

7 Linac technology issues for superconducting standing wave structures

SC SW structures are typically multi-cell structures (up to 10 cells) working in the π mode. The cell irises are designed with an elliptical shape to minimize the ratio between the surface electric field and the accelerating one, E_{surf}/E_{acc}. The surface electric field, in fact, has to be minimized to avoid electron field emission processes that can limit cavity performance at a high gradient. The elliptical shape of the cell is chosen to minimize the ratio between the surface magnetic field and the accelerating one, B_{surf}/E_{acc}. As already pointed out, the ultimate limit for the maximum achievable gradient in SC structures is due to the critical magnetic field that for Nb is ~170 mT to 180 mT. For the TESLA cavities [6, 29, 30], since this ratio is $B_{surf}/E_{acc} \cong 4.2\,\mathrm{mT/MV/m}$ the maximum theoretical achievable accelerating field is about 50 MV/m.

The elliptical shape is also useful for suppressing multipacting phenomena that can limit cavity performance at a high gradient, while large irises also increase the machinability and cleanability of the cavities. The sketch of the cell profile of the TESLA cavities is shown in Fig. 29, while the *r/Q* and surface field are plotted as a function of the irises radius in Fig. 30 [29, 30].
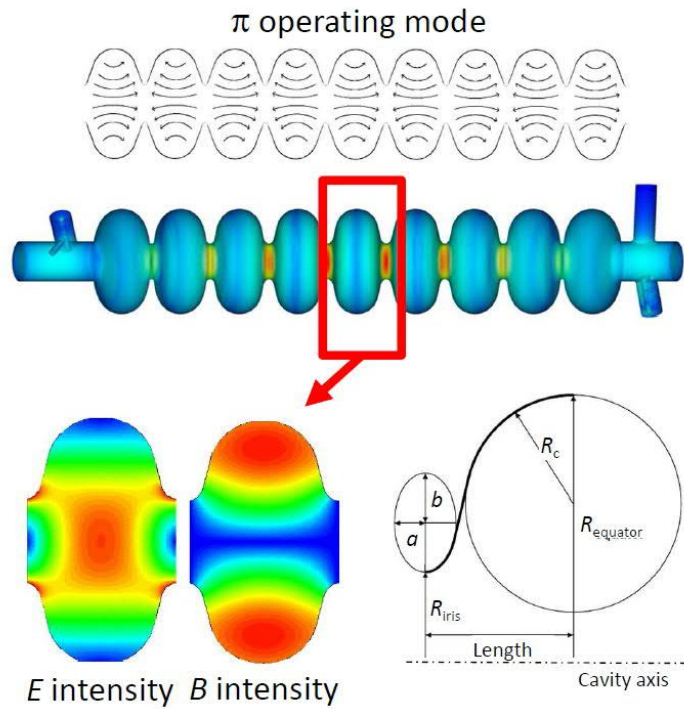
Fig. 29: Sketch of the cell profile of the TESLA cavities (courtesy [6, 29, 30])
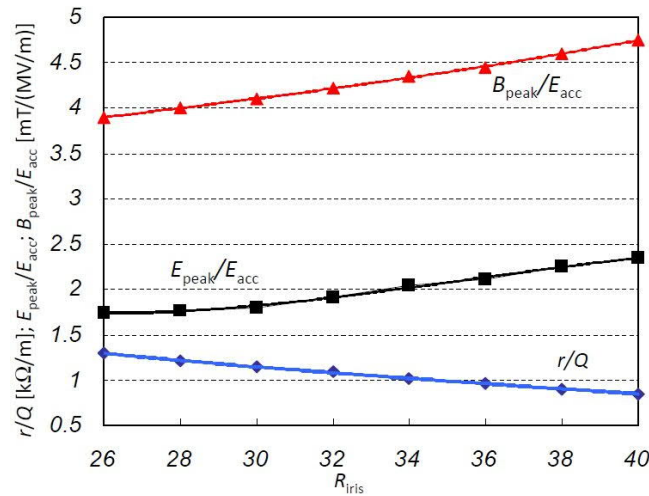
Fig. 30: r/Q, E_{surf}/E_{acc} and B_{surf}/E_{acc} as a function of the irises' radius (TESLA cavities, courtesy [29, 30])

SW SC cavities are typically powered by coaxial-type couplers [3, 31]. Magnetic coupling with waveguides or loops is also possible, but it can create hot spots in the cavities with additional complications in the design. The inner conductor of the coaxial is coupled to the electric field at the end of the structure. Coaxial couplers allow variation of the coupling strength by changing the penetration of the couplers into the cavity itself. For instance, this is necessary for accelerators that operate at different beam currents. The couplers also have vacuum barriers (windows) to prevent contamination of the SC structure. Obviously these barriers are also necessary in normally conducting accelerators, but the demands on the quality of the vacuum and reliability of the windows are less stringent than for SC cavities. The failure of a window in a superconducting accelerator could imply very expensive and time-consuming repairs. These windows are generally made from Al_2O_3. Ceramic material has also a high SEY that stimulates multipacting activity, and to reduce this phenomena Ti coatings on the surface of the ceramic are frequently used. Finally, the couplers must constitute a thermal barrier since they are at

the boundary between room temperature and the cryogenic temperature environment. The final drawing of a SC coupler is therefore very complex, as shown in Fig. 31, where the TESLA coupler is presented [6].
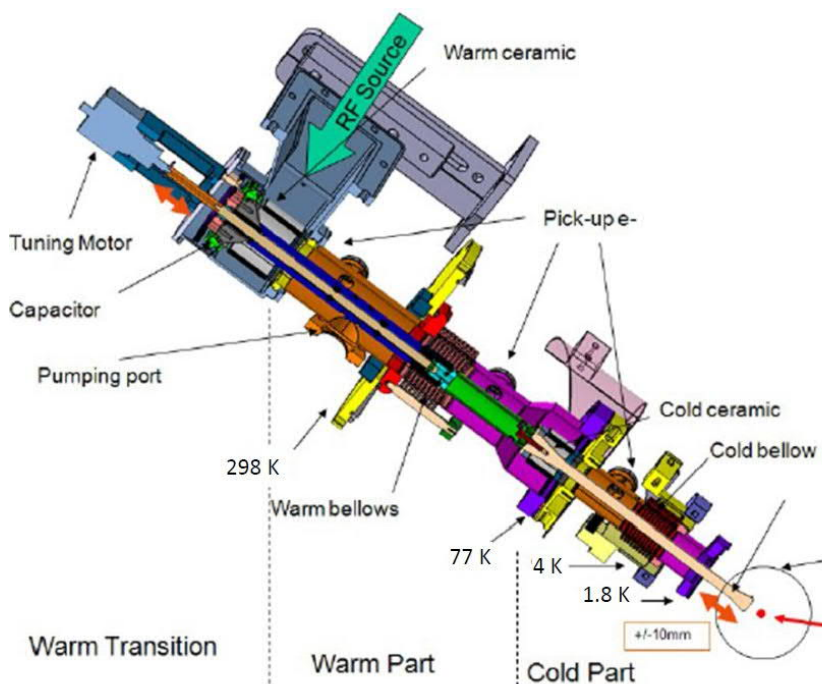

Fig. 31: Mechanical drawing of the TESLA coupler

As already pointed out, SC cavities are suitable for the acceleration of trains of bunches. As a bunch traverses a cavity, however, it deposits EM energy on Higher Order Modes (HOM), described in terms of long-range wakefields. Subsequent bunches (or the same bunch in several turns, as in ERLs) may be affected by these fields, causing beam instabilities and additional heating of accelerator components. As an example, the sketch of the field excited by one bunch passage into a TESLA cavity is reported in Fig. 32. To absorb the excited EM field several approaches can be used, such as loop couplers, waveguide dampers or beam pipe absorbers [31]. In all the above mentioned options, only the fields excited by the beam are absorbed, while the accelerating mode is rejected by EM filters and remains unperturbed. For instance, for a waveguide absorber the cutoff frequency of the waveguide is higher than the working frequency of the operating mode, thus it cannot propagate into the waveguide itself. When loops are used, notch filters are inserted to decouple the working mode from the coaxial. Pictures and drawings of different kind of such devices are shown in Fig. 33.
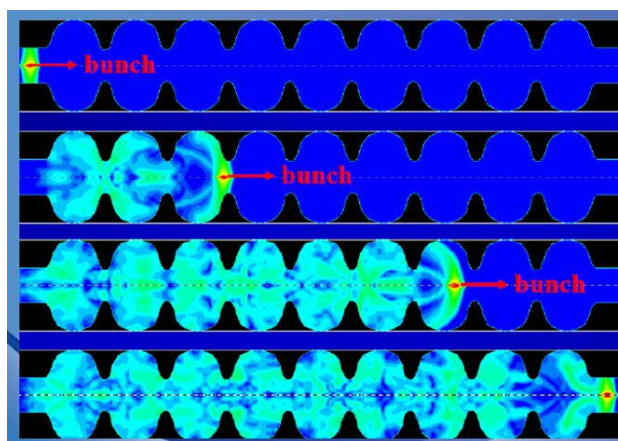

Fig. 32: Sketch of the field excited by the bunch passage into the cells of a TESLA cavity (courtesy [21])
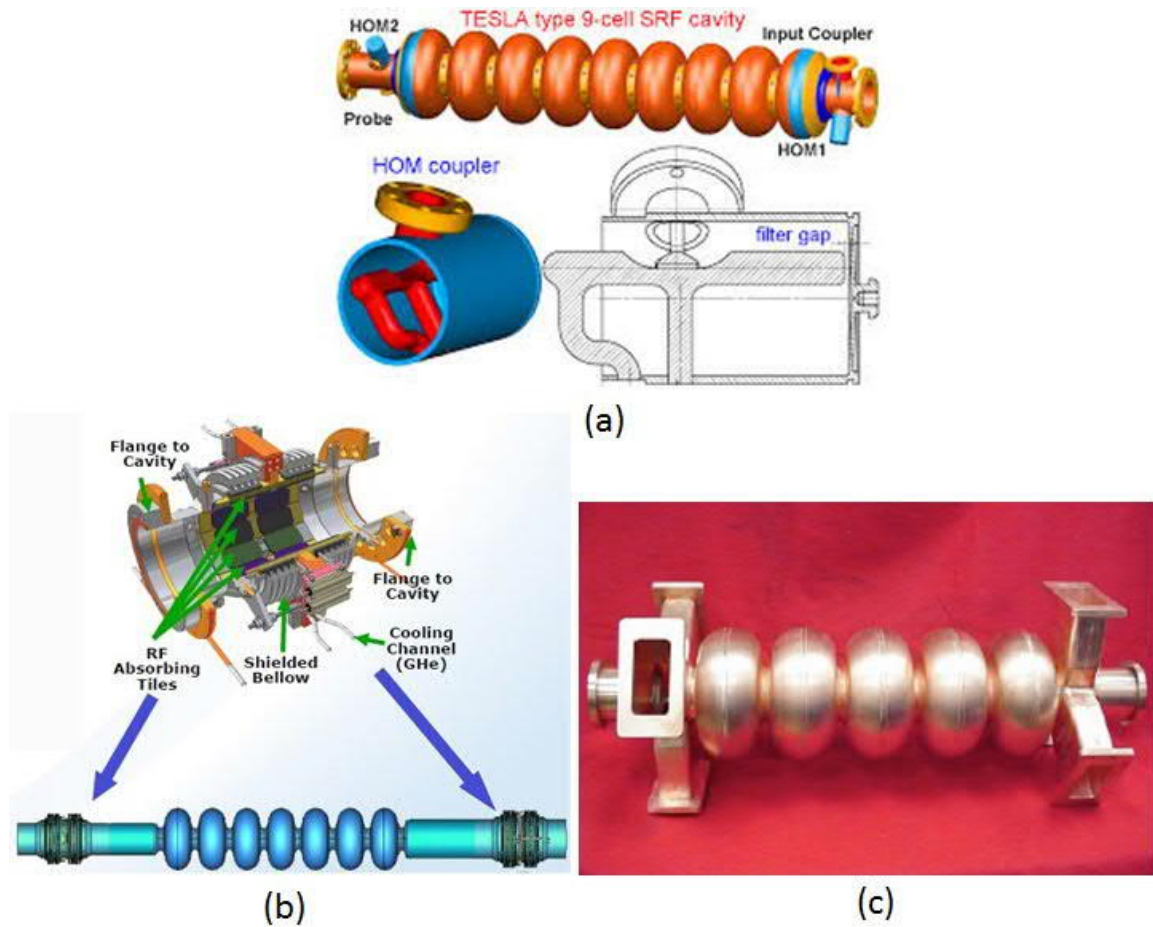
Fig. 33: Pictures and drawings of different types of HOM damping systems: (a) loop couplers, (b) waveguide dampers; (c) beam pipe absorbers (courtesy [21]).

Niobium is available as a bulk and sheet material in any size, fabricated by forging and rolling. High purity Niobium is made by electron beam melting under a good vacuum. The most common fabrication techniques for the cavities are deep drawing or spinning half-cells [21–23]. These processes are schematically represented in Fig. 34.
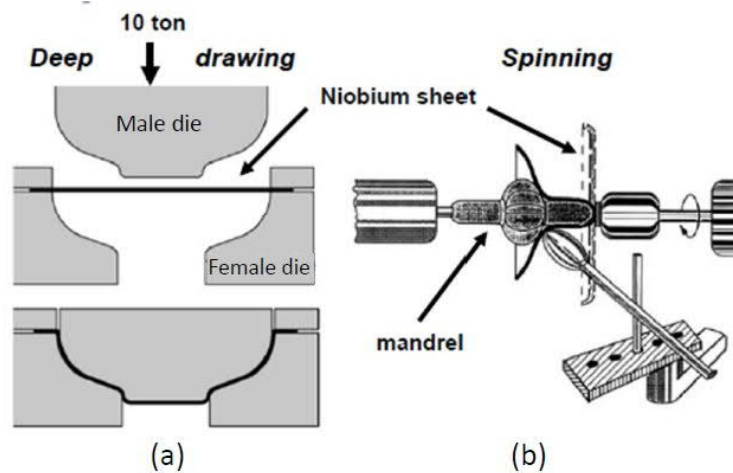
Fig. 34: Most common fabrication techniques for SC cavities: (a) deep drawing; and (b) spinning half-cells

Typically, the cells of the cavity are electron-beam welded and they undergo a long, and very delicate, process of polishing and cleaning [22, 23, 32, 33]. The cavity treatment requires several steps in between, such as buffered chemical polishing (BCP), electro-polishing and etching, which allows the removal of surface damaged layers of the order of ~100 μm. The cavities are rinsed with ultraclean water at high pressure (~100 bar) for several hours to remove the residual acid used for treatment. They also undergo a thermal treatment (with temperatures higher than 1000°C) to diffuse H_2 out of the material, increasing the purity of the niobium. During and after these treatments the cavities have to be maintained in a very clean environment, to avoid contamination that can limit their performances during high-power operation. Before the final cleaning process, the cavities are also characterized and tuned with low power RF. A picture of some cavities during the assembly process in a clean room is shown in Fig. 35. In general, the process of fabrication is not unique, and companies, industries or laboratories adopt their own developed techniques.


**Fig. 35:** Cavities during the assembly process in a clean room

After their construction and assembly, the cavities under vacuum, or in a controlled N_2 atmosphere, are inserted and assembled into the cryomodules. In the cryomodules the cavity is immersed in a liquid helium bath, which is pumped to remove helium vapour boil-off, as well as to reduce the bath temperature.

The cold portions of the cryomodule need to be extremely well insulated, which is best accomplished by a vacuum vessel surrounding the helium vessel and all ancillary cold components.

A schematic of a cryomodule is given in Fig. 36, while a picture of an XFEL cryomodule is shown in Fig. 37 with its mechanical cross-section. A single cryomodule can incorporate several cavities, as in the XFEL in Fig. 38, where eight cavities are integrated with bellows beam position monitors (BPMs) and quadrupoles.
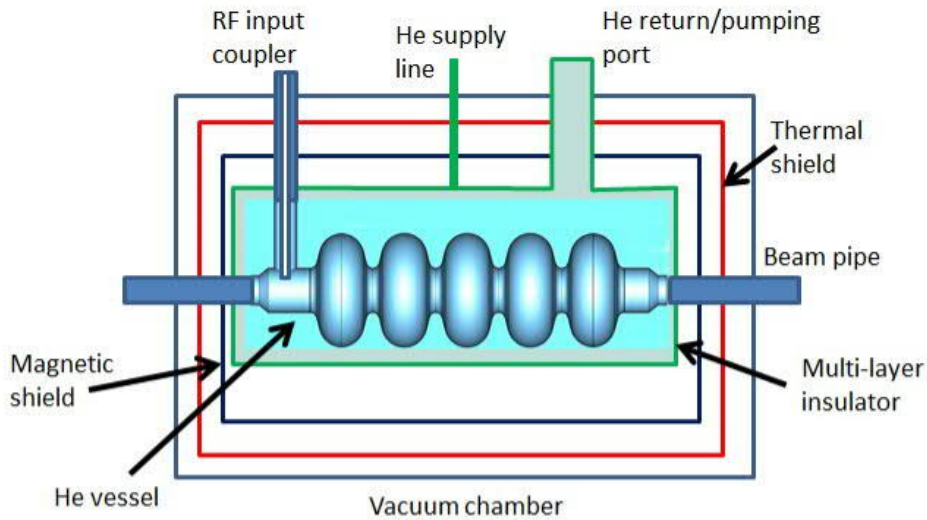
Fig. 36: Schematic of a cryomodule
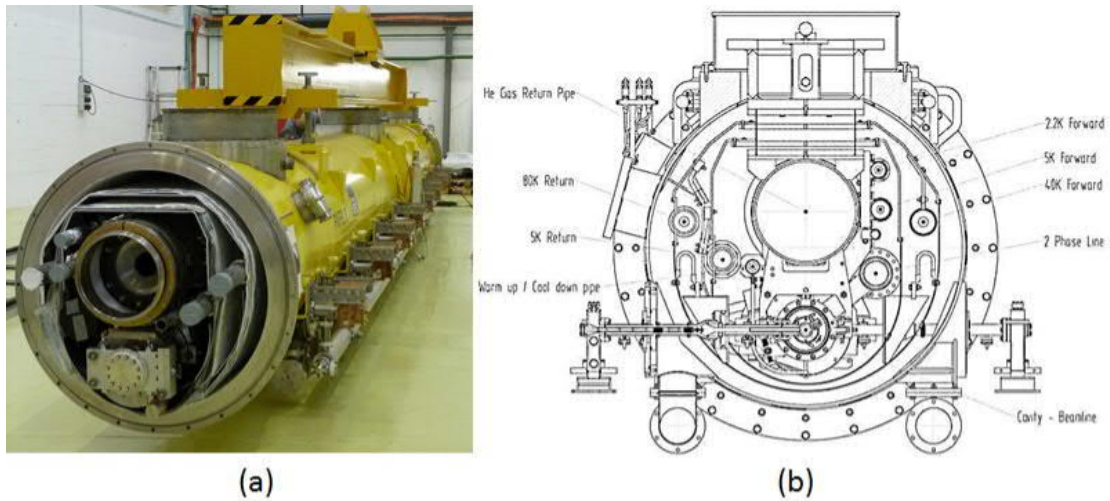
Fig. 37: (a) Picture of the XFEL cryomodule; (b) mechanical cross-section
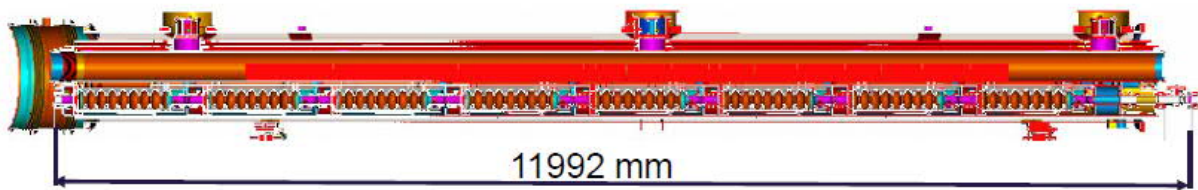
Fig. 38: XFEL cryomodule integrating eight cavities, bellows BPMs and quadrupoles

The requirements for the stability of the accelerating field in a superconducting structure are comparable to those of a normal conducting cavity. The nature and magnitude of the perturbations to be controlled, however, are rather different. Superconducting cavities have a very narrow bandwidth and are, therefore, highly sensitive to mechanical perturbations. Therefore, significant phase and amplitude errors may be induced by frequency variations. Perturbations can be excited by mechanical vibrations (microphonics), changes in helium pressure and level, or Lorentz forces. Slow changes in frequency, on a timescale of minutes or longer, can be corrected by a frequency tuner, while faster changes must be counteracted by an amplitude and phase modulation of the incident RF power. A schematic drawing of the RF system feeding a SC cavity is given in Fig. 39. The signals are measured from the pickup and

are the inputs of the low level RF (LLRF) system, which allows the input to be kept linked to the resonant frequency of the cavity. Circulators are also needed to prevent damage to the klystron due to the reflected power from the cavities, as pointed out above.
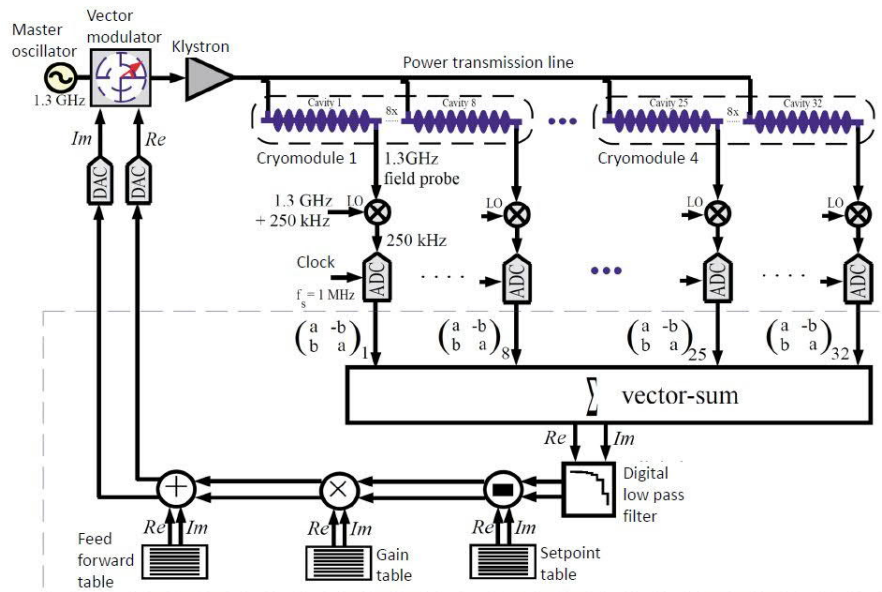

Fig. 39: Schematic drawing of the RF system feeding a SC cavity (courtesy [6])

8   Performances of different type of structures at a high accelerating field

If properly cleaned and fabricated, TW NC cavities can quite easily reach a relatively high gradient (>40 MV/m) without particular limitations. After less than one hundred million pulses (a few hundred hours at 100 Hz repetition rate) of conditioning, in which the power and pulse length are progressively increased, they can usually reach their nominal performance. The main limitation comes from breakdown phenomena, whose physics interpretation and modelling is still under study and is not yet completely understood. The goal of the conditioning process is to expose the internal surface of the component to ramped RF power in order to clean it. Several effects contribute to surface cleaning: induced out-gassing due to RF heating, arcing and multipacting (which enhance local heating) and desorption. To avoid damage to the structure, RF conditioning must be carried out gradually and in a controlled way. Generally, during the process different parameters are monitored, such as vacuum level, and forward, reflected and transmitted RF power. These parameters are used to verify the conditioning progress and to generate interlocks, in order to protect the machine components in case of breakdown.

At full performance, S-band cavities can operate without breakdowns at gradients of up to 25 MV/m to 30 MV/m, while C-band cavities can even reach higher gradients. So far, high gradient tests on C-band structures have been successfully carried out at up to 50 MV/m. In the X-band (12 GHz) higher gradients can be reached (>100 MV/m). Nevertheless, at present, FEL linacs do not operate at these frequencies due to the higher cost of power sources and more critical issues related to fabrication, tolerances, alignments, pumping systems, etc. In principle, a very high gradient (up to the level of the X-band structures) can be reached at lower frequencies (S- or C-band) as well. In these cases, however, the main limitation is the lower shunt impedance, which requires a higher power per unit length to sustain such gradients. A typical behaviour of the conditioning process for a TW structure (Extreme Light Infrastructure-Nuclear Physics, ELI-NP, C-band) is shown in Fig. 40, where the pulse length, the structure input power and the repetition rate are reported as a function of time (hours). As can be noted from Fig. 40, after about 150 hours of conditioning the structure reached its final level of performance [34].
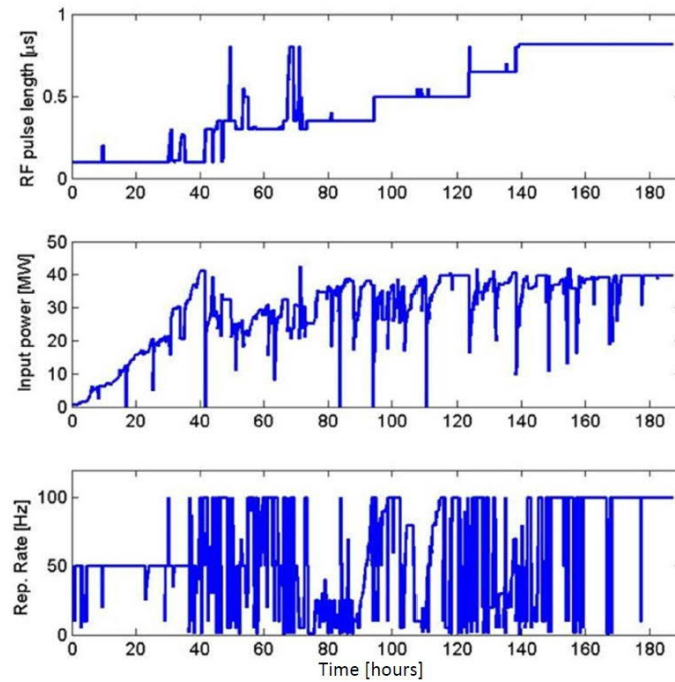
Fig. 40: An example of typical behaviour during the conditioning process for a TW structure (ELI-NP C-band)

SC cavities also need to be conditioned and, their performance is usually analysed by plotting the behaviour of the quality factor as a function of the accelerating field [35]. A typical plot is reported in Fig. 41, where the dots represent the measured points with respect to the ideal case (solid line). There are several phenomena responsible for additional losses under high power, which causes the quality factor to be lower than expected.

First, as already pointed out, the measured surface resistivity is typically larger than that predicted by Bardeen–Cooper–Schrieffer (BCS) theory. This is due to magnetic flux trapped in the cool-down process, dielectric surface contaminations (chemical residues, dust…), defects and inclusions, surface imperfections and hydrogen precipitates. This increase in losses can be limited by very clean and careful cavity fabrication, e.g. using ultra-pure Nb, cleaning processes and thermal cavity treatments.

At an intermediate level of field, multipacting phenomena can occur [15]. Multipacting is a resonant process that occurs when a large number of electrons build up under the influence of an RF field. It can occur either in the regions of input couplers or in cavity cells. Basically, it starts from a process of electron field emission. The emitted electrons start to hit the surfaces, emitting more electrons, and so on. Two main conditions are needed to activate the electron build-up: electron synchronization with the RF field and electron multiplication via secondary emission (SEY). Multipacting was an early limitation of SC cavities performance and it was overcome by adopting spherical or elliptical cell shapes. These allow modification of the electrons' trajectories, reducing surface collisions and the synchronicity with the RF field. RF conditioning can also reduce multipacting. Figure 42(a) shows typical electron trajectories when RF fields are applied, while Fig. 42(b) reports the SEY as a function of the impact energies of electrons for a cavity with several different treatments.
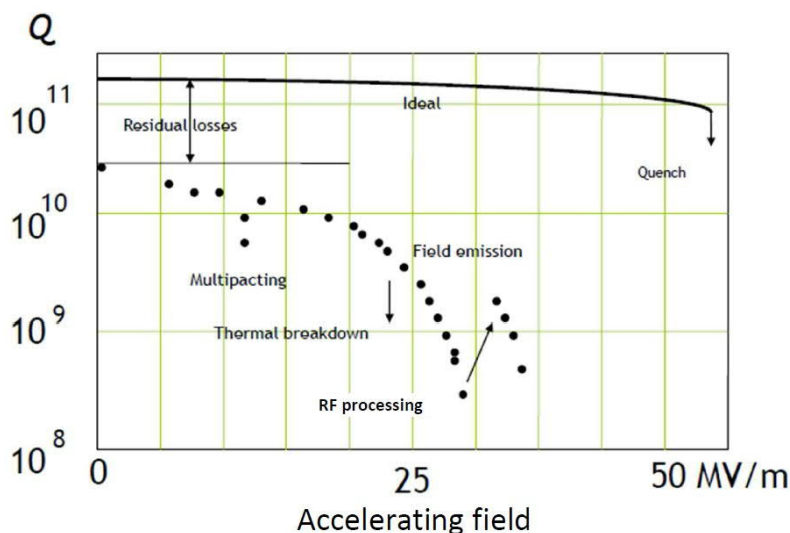
Fig. 41: Typical behaviour of the quality factor of a SC cavity as a function of the accelerating field (courtesy [35])
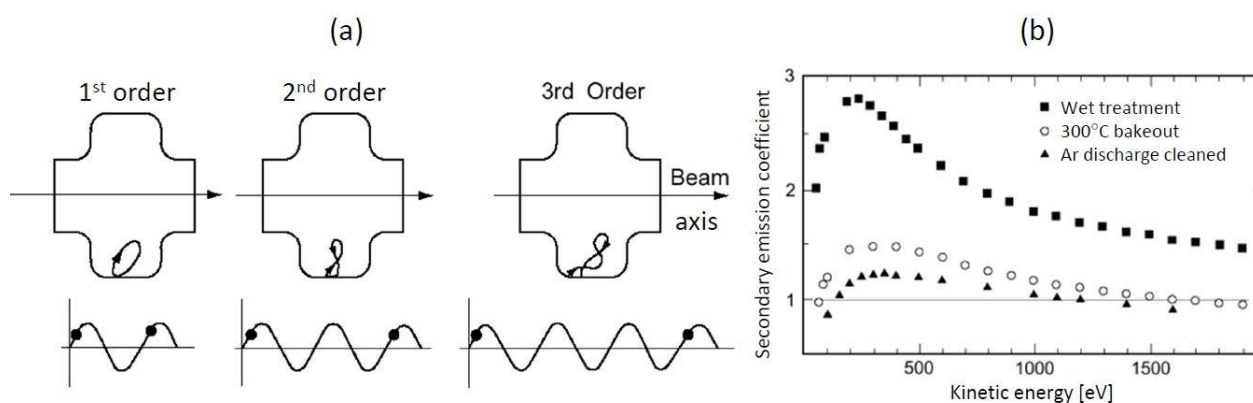
Fig. 42: (a) Typical electron trajectories under RF field that causes hitting of the surface by emitted electrons; (b) SEY as a function of the impact energies of electrons for a cavity with several different treatments (courtesy [35]).

At high fields, thermal breakdown can also occur when the heat generated in one hotspot (e.g. due to impurities or defects) is larger than can be transferred to the helium bath. This causes an increase of the temperature above the critical temperature (T_c) and, consequently, a 'quench' of the superconducting state. The mechanism is schematically illustrated in Fig. 43.

The last phenomenon we want to mention is the exponential increase of losses due to the acceleration of field-emitted (FE) electrons, which is also associated with the production of X-rays and dark current. This mechanism is illustrated in Fig. 44. The main cause of FE is particulate contamination. FE can be prevented by proper surface preparation and contamination control. It is possible to reduce it also using High-power Pulsed Processing (HPP) and/or helium processing.
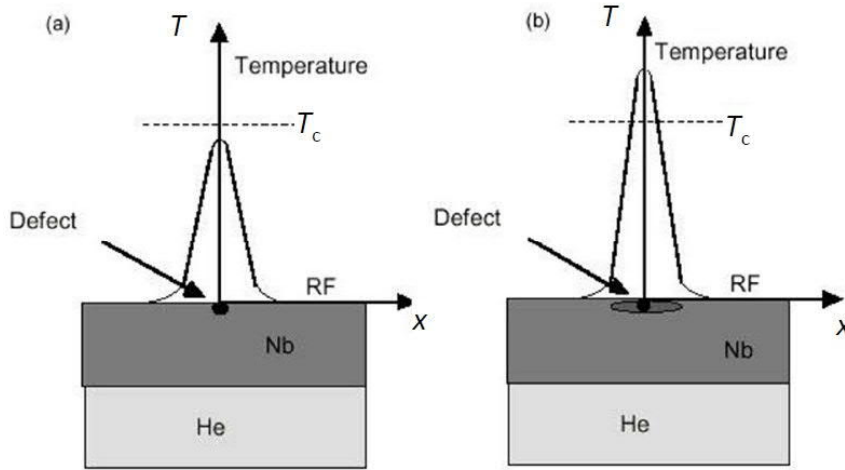
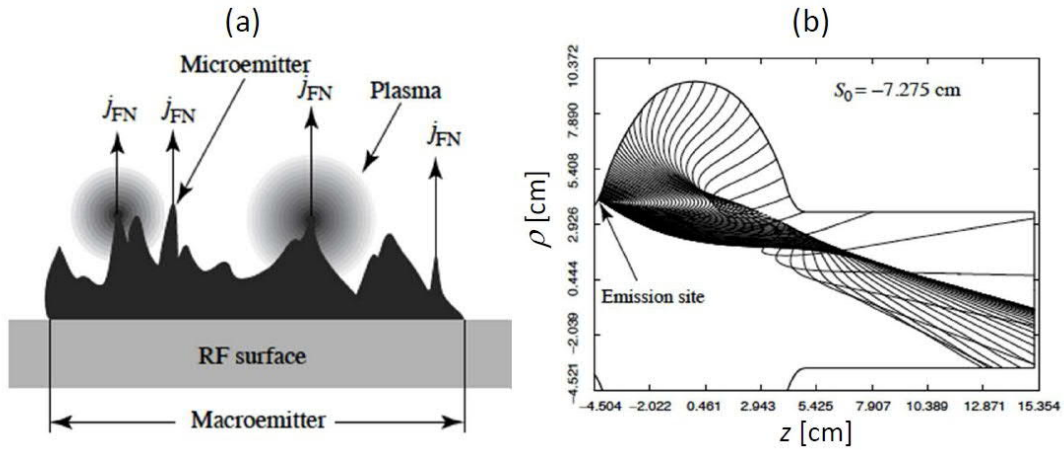**Fig. 43:** Thermal breakdown schematic representation (courtesy [35])

Fig. 44: FE process: (a) the emission of electrons is enhanced by the presence of surface defects of spikes; (b) emitted electrons hit the surface causing X-rays emission and heating (courtesy [21]).

9   Electron sources

There are different types of electron sources. A complete treatment can be found in [36]. Here we want to mention only a couple that may be used for different applications in FEL and ERL.

### 9.1   Radio frequency photo-guns

Radio frequency photo-guns are used as electron sources and for the first acceleration stages in FEL. They are multi-cell structures, typically made from one to three cells. The geometry of a 1.6 cell RF gun with its electric field lines is given in Fig. 45. The device is powered by a waveguide and a coupling hole on the full cell. These structures typically operate in the π mode, and the electrons are emitted by a cathode, whose surface is hit by a laser (working usually in the UV, e.g. at 240 nm to 260 nm). Electrons are extracted by means of the photo-electric effect, and then accelerated by an electric field that is designed to have a longitudinal component on the gun's axis. They enter the full cell, where they are further accelerated. RF guns can operate in the L- or S-band (i.e. from ~1 GHz to ~3 GHz) at repetition rates upto 100 Hz and above. The cathode peak field is typically of the order of 60 MV/m to 120 MV/m. The RF pulse length can be a few microseconds (S-band) up to hundreds of milliseconds (L-band). The number of emitted electrons is proportional to the laser power and quantum efficiency (QE) of the

cathode material [36]. QE is given by the ratio between the number of emitted electrons and the number of incident photons (QE of copper cathodes is in the range 10^{-5} to 10^{-4}). The cathodes can be of different type: copper (as is the bulk of the gun) or other materials with a higher QE (for instance GaAs). The mechanical design of the gun has to allow for the possibility of substituting the cathode itself in case of deterioration or damage.
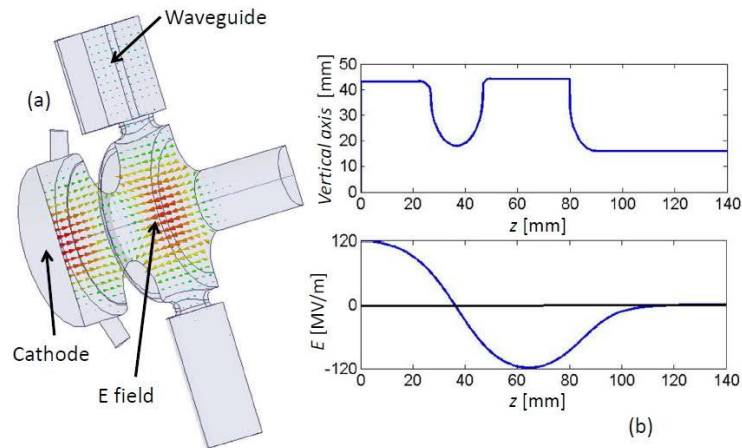

Fig. 45: (a) Geometry of a 1.6 cell RF gun with electric field lines; (b) profile along the longitudinal axis

The mechanical drawing of the ELI-NP RF gun [37] is given in Fig. 46(a) with a picture of the main components before assembly and brazing (Fig. 46(b)). Figure 47 shows the RF gun installed with the solenoid immediately after the accelerating cells for emittance compensation and control. The conceptual scheme of the laser system and photo gun is given in Fig. 48. Figure 49(b) shows a picture of the LCLS photo-gun together with the power splitter, which is needed to symmetrize the power feed to avoid dipole kicks due to the coupler holes. The main LCLS gun parameters are summarized in Table 4 [38–40].
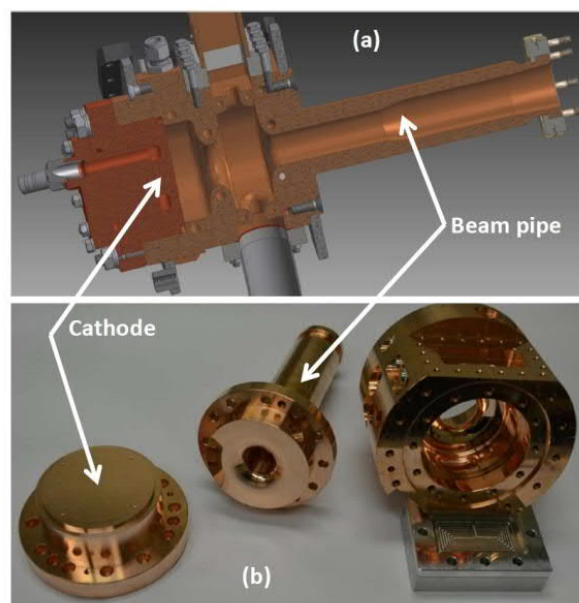
Fig. 46: (a) Mechanical drawing of an RF gun; (b) pictures of the main components before assembly
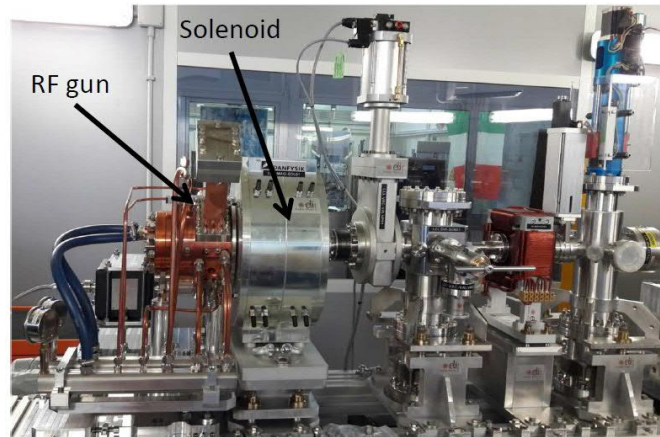
Fig. 47: RF gun installed with the solenoid immediately after the accelerating cells for emittance compensation
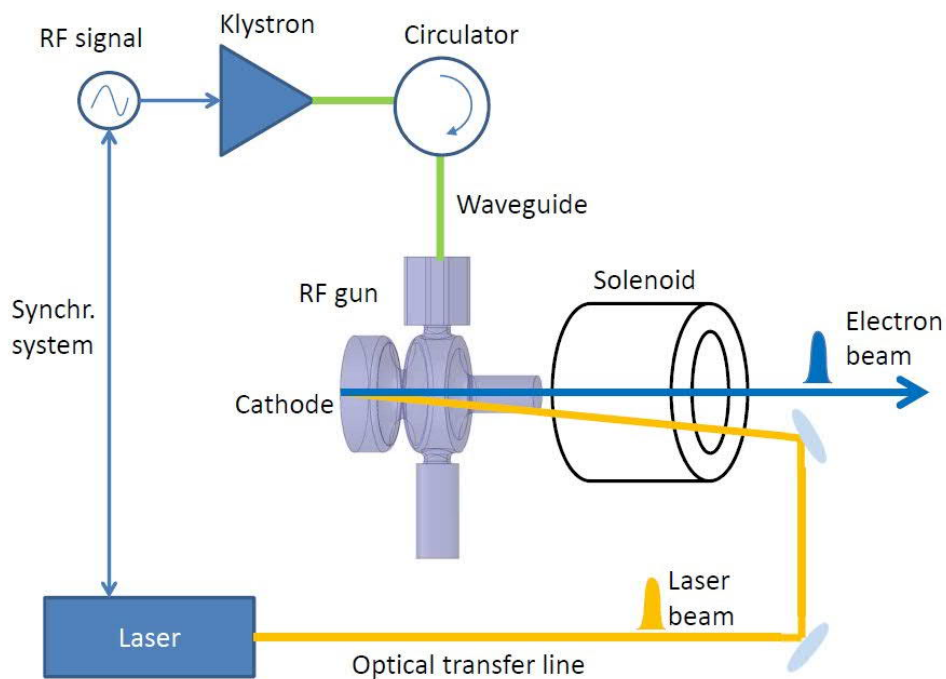

Fig. 48: Conceptual scheme of the laser system and photo-gun

Figure 49(a) shows the PITS L-band gun of the XFEL [5, 41, 42]. Two solenoids are foreseen to completely cancel the magnetic field on the cathode, which can increase the beam emittance. The main parameters are given in Table 4.

Table 4: Main LCLS and PITZ gun parameters

Parameter	LCLS gun	PITZ gun
Frequency [GHz]	2.856	1.3
Number of cells	1.6	1.5
Cathode peak field [MV/m]	120	60
Photocathode type	Cu	Cs_2Te
Repetition rate [Hz]	120	10
Number of bunches per RF pulse	1	<2700
RF pulse length	~2 μs	<700 μs
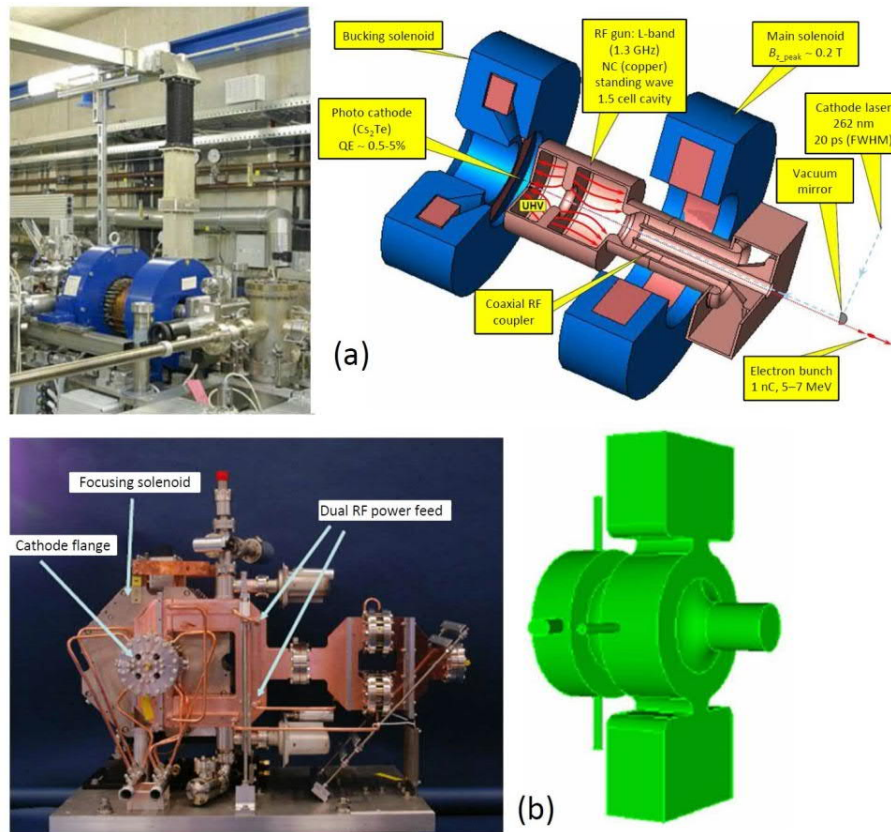
Fig. 49: (a) PITS L-band gun of the XFEL; (b) picture of the LCLS photo-gun with the big splitter to symmetrize the feeding avoiding dipole kick.

9.2 Direct Current photo-guns

Direct current (DC) photo-guns can be used as electron sources for high average current accelerators (CW operation, high Duty Cycle linac, typically ERL). The cathode must have a high QE (as example for GaAs QE is a few percent) and is illuminated by a continuous train of laser pulses. Average currents up to 100 mA can be achieved with this kind of source. A mechanical drawing of the Cornell DC gun [43] is given in Fig. 50, with the main parameters reported in Table 5. DC photo-guns are characterized by an electron energy that is lower than that of RF photo-guns. This is due to the lower accelerating gradient that is possible to achieve in the DC regime; post-acceleration and beam manipulation are then required to reach the desired beam energy and performance. As an example, Fig. 50(b) shows the line after the Cornell DC gun, made from two emittance compensation solenoids and a 1.3 GHz normal conducting bunching cavity. These elements are used to compensate the initial emittance blowup near the cathode, and to compress the bunch longitudinally before further acceleration. The bunches are then accelerated using five superconducting niobium cavities. This multi-cell cavity allows the partial freezing of the emittance, to increase the energy and to perform further emittance compensation and longitudinal compression via time-dependent transverse and longitudinal focusing.
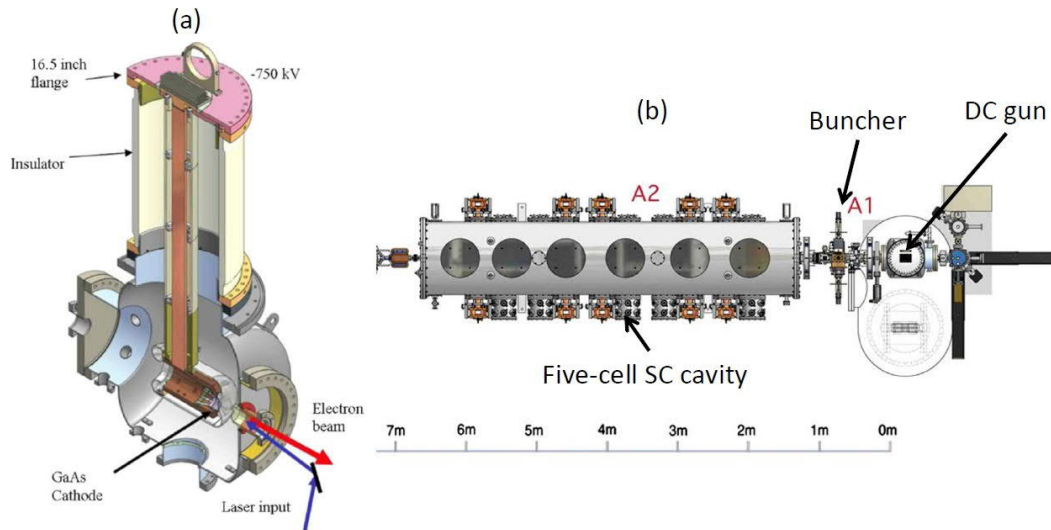
Fig. 50: (a) Mechanical drawing of the Cornell DC gun; (b) layout of the complete Cornell injector

**Table 5:** Main Cornell injector design parameters

Parameter	Value
Beam energy [MeV]	5 to 15
Normalized emittance [μm]	≤0.3
Bunch length [ps]	≤3 ps
Photocathode type	GaAs
DC accelerating voltage [kV]	500 to 600
Average current [mA]	100
Bunch charge [pC]	77
Bunch frequency [GHz]	1.3

10   Power sources and power distribution systems

RF power sources would require a dedicated treatment. A comprehensive description can be found, for example, in [44–46]. In this paper, for sake of completeness, we report some useful information.

### 10.1   Klystron, inductive output tube and solid-state amplifiers

The most common RF power sources are klystrons. They allow pulsed or CW operation and can work from hundreds of megahertz up to tens of gigahertz, generating peak power, in the low DC pulsed regime, up to several tens of MW. A sketch of a klystron is given in Fig. 51(a). A high DC voltage (hundreds of kV) is applied between a cathode and an anode through special devices called modulators. The DC current (up to more than 100 A) emitted by the cathode filament is then accelerated by the DC voltage and is bunched through a system of cavities. The first input cavity is fed with a driver signal that starts this bunching process, while the last output cavity is excited by the bunched beam and is coupled to a waveguide that collects the produced RF power. Finally, the collector absorbs the beam. The signal from the RF driver is, in conclusion, amplified more than 40 dB.
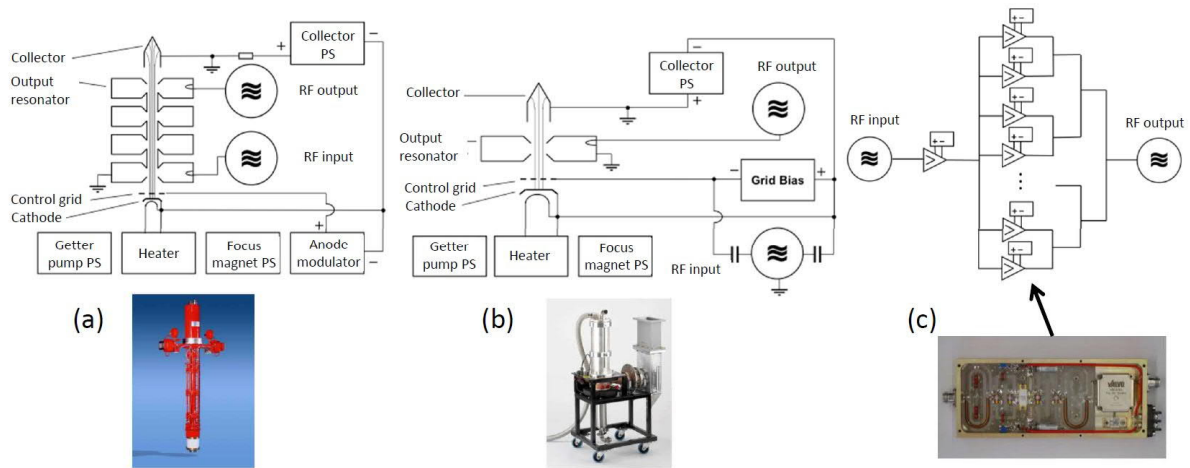
Fig. 51: (a) Sketch of a klystron; (b) schematic of an IOT; (c) schematic principle of a solid-state amplifier

At lower power (up to hundreds of kilowatts) the Inductive Output Tube (IOT) can also be used. A schematic of an IOT is given in Fig. 51(b). The intensity modulation of the DC beam is realized by a control grid. These devices can typically operate at up to 2 GHz and, in general, their efficiency is larger than that of klystrons.

Finally, solid-state amplifiers can also be used at frequencies lower than 2 GHz. A schematic of the principle of such devices is shown in Fig. 51(c). The power of many transistors is combined. The advantage of this system, with respect to vacuum tubes, is the compactness and the possibility to operate even if a single module fails. In fact, we have a reduction just of the output power. Concerning their efficiency, they can also exceed that of vacuum tubes. On the other hand, they allow operation at moderate power. Finally, Fig. 52 gives an overview of the maximum power and frequency for the different types of source.
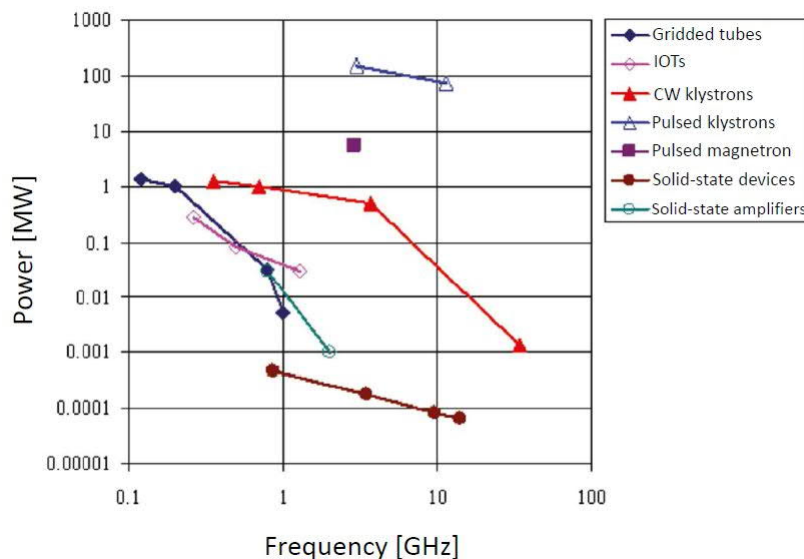

Fig. 52: Overview of the maximum power and frequency for the different type of sources (courtesy [45])

10.2 Pulse compressor systems: SLAC Energy Doubler (SLED)

As pointed out above, TW structures have to be fed by short, high peak power pulses. One way to achieve this is the energy doubler that was invented and implemented for the first time in the SLAC linac [47]. The principle of operation is given in Fig. 53. Basically, the power from the klystron is stored in special cavities and then abruptly released to the accelerator. More precisely, the waveguide system

is connected through a 3 dB coupler to a pair of two cavities with a high quality factor ($>10^5$). At the beginning of the RF pulse, part of the klystron power goes into the cavities, building them up, while the remainder is reflected and through the 3 dB coupler is sent to the accelerator. As the stored cavity fields increase they radiate power in counter-phase with the incident power so that the mean power transmitted to the accelerator decreases. The cavities are over-coupled so that the peak reflected power rises to a level greater than the transmitted power. At a certain time (t_{switch}) the phase of the klystron drive is abruptly reversed and the reflected and transmitted signals are then in phase, causing a fast increase of the actual power transmitted to the accelerator, at the expense of pulse duration. A picture of the C-band SLED implemented in the Spring-8 FEL is given in Fig. 54.
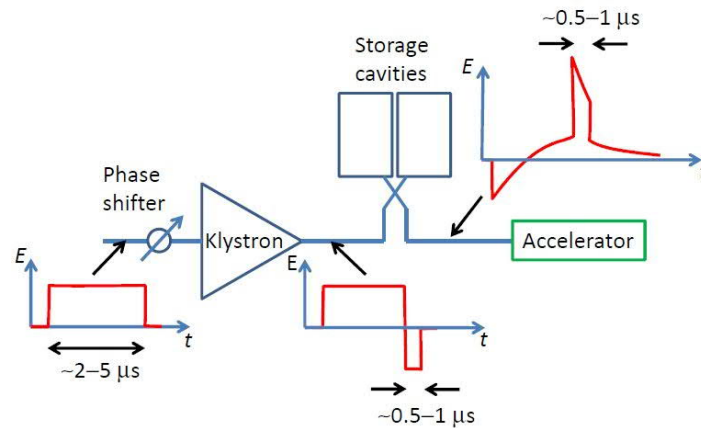
**Fig. 53:** Schematic layout of a SLED system

Fig. 54: Picture of the C-band SLED system implemented at Spring 8 [13, 14]

10.3 Waveguide power distribution systems

A treatment on linac technology cannot exclude a very quick overview on waveguide components that allow the transport and distribution of RF power from the source to the accelerator devices. A few of these components are shown in Fig. 55. Amongst others, we can mention the following [46].

i) Circulator (or isolator) that allows protection of the RF source from reflections due to the powering of SW structures. The circulator is a passive non-reciprocal device with three ports, and protects (isolates) the RF power sources from microwave power reflected back from non-ideal loads. This is possible due to the unique magnetic properties of ferrites that, when properly magnetized, introduce different phase shift for EM waves travelling in opposite directions.

ii) Attenuator and phase shifters that allow changes, at high power, to the phase or the power level.

iii) Directional couplers that allow the measurement of the power flowing into the waveguide in both directions (forward and reflected).

iv) Pumping ports to evacuate the waveguide and reach a vacuum level of the order of 10^{-8} mbar.

v) Ceramic windows that allow separation of the vacuum of the linac from that of the waveguides (which are generally at a higher pressure than that of the linac). Moreover, in the case of an intervention, one has to vent only a limited part of the accelerator. Several components like phase shifters, attenuators and circulators have to operate in a controlled atmosphere with gases with a high dielectric rigidity (like SF6). Ceramic windows allow the separation of the vacuum of the linac or waveguides from these regions.

vi) Bends and splitters that allow distribution of power from the source.
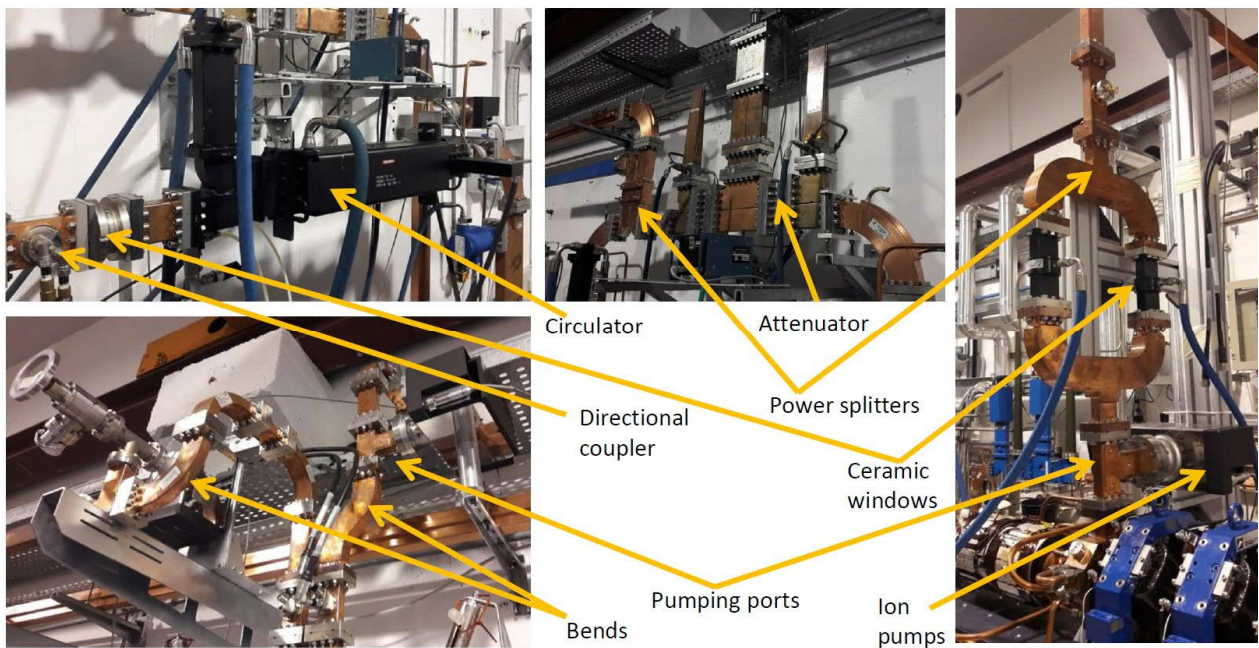
Fig. 55: Pictures of waveguide components

Acknowledgements

References

[1] E. Jensen, Cavity basics, in Proceedings of the CAS–CERN Accelerator School: RF for Accelerators, Ebeltoft, Denmark, 8–17 June 2010, CERN-2011-007 (CERN, Geneva, 2010) pp. 259–275, arXiv:1201.3202.

[2] F. Gerigk, Cavity types, in Proceedings of the CAS–CERN Accelerator School: RF for Accelerators, Ebeltoft, Denmark, 8–17 June 2010, CERN-2011-007 (CERN, Geneva, 2010), pp. 277–298, arXiv:1111.4897.

[3] D. Alesini, Power coupling, in Proceedings of the CAS–CERN Accelerator School: RF for Accelerators, Ebeltoft, Denmark, 8–17 June 2010, CERN-2011-007 (CERN, Geneva, 2010), pp.125–147, arXiv:1112.3201.

[4] T. Wangler, *RF Linear Accelerators* (Wiley, New York, 1998). https://doi.org/10.1002/9783527618408

[5] DESY, Technical Design Report (TDR) of the European XFEL, 2007, http://xfel.desy.de/technical_information/tdr/tdr/.

[6] B. Aune *et al.*, *Phys. Rev. ST Accel. Beams* **3**(9) (2000) 092001. https://doi.org/10.1103/PhysRevSTAB.3.092001

[7] R.E. Collin, *Foundations for Microwave Engineering*, 2nd ed. (McGraw-Hill, Singapore, 1992).

[8] R.B. Neal, *The Stanford Two-Mile Accelerator* (Benjamin, New York, 1968).

[9] T. Garvey, The SwissFEL Linac (2014), http://www-pnp.physics.ox.ac.uk/~jaiweb/slides/2014_Garvey.pdf.

[10] R. Zennaro *et al.*, Measurements and high power test of the first C-band accelerating structure for SwissFEL, Proc. LINAC2014, Geneva, Switzerland, (Jacow, CERN, Geneva, 2014) p. 333.

[11] J.-Y. Raguin and M. Bopp, The Swiss FEL C-band accelerating structure: RF design and thermal analysis, Proc. LINAC2012, Tel-Aviv, Israel, (Jacow, CERN, Geneva, 2013), p. 501.

[12] R. Ganter, SwissFEL status report, Proc. FEL2015, Daejeon, Korea 2015, (Jacow, CERN, Geneva, 2015), p. 567.

[13] T. Inagaki *et al.*, *Phys. Rev. ST Accel. Beams* **17**(8) (2014) 080702. https://doi.org/10.1103/PhysRevSTAB.17.080702

[14] K. Okihira, Mass production report of C-band choke mode accelerating structure and RF pulse compressor, Proc. IPAC2011, San Sebastián, Spain, 2011, (EPS-AG, Geneva, 2011), p. 668.

[15] R. Parodi, Multipacting, in Proceedings of the CAS–CERN Accelerator School: RF for Accelerators, Ebeltoft, Denmark, 8–17 June 2010, CERN-2011-007 (CERN, Geneva, 2010), pp.447–458, arXiv:1112.2176. http://dx.doi.org/10.5170/CERN-2011-007.

[16] D.C. Mattis and J. Bardeen, *Phys. Rev.* **111**(2) (1958) 412. https://doi.org/10.1103/PhysRev.111.412

[17] H. Padamsee. RF *Superconductivity: Science, Technology, and Applications* (Wiley-VCH, Weinheim, 2009). https://doi.org/10.1002/9783527627172

[18] H. Padamsee, J. Knobloch, and T. Hays. *RF Superconductivity for Accelerators* (Wiley, New York, 1998).

[19] H. Safa, Surface effects in SCRF cavity, in Proceedings of the CAS–CERN Superconductivity and Cryogenics for Accelerators and Detectors, Erice, 2002, CERN 2004-008 (CERN, Geneva, 2004), p. 196. http://dx.doi.org/10.5170/CERN-2004-008

[20] G. Bisoffi, Superconducting cavities, in Proceedings of the CAS School on Radiofrequency Engineering, CERN 2005-003 (CERN, Geneva, 2005), p. 315. http://cdsweb.cern.ch/record/386544/files/CERN-2005-003.pdf.

[21] S. Belomestnykh, Principles of RF superconductivity, lecture at USPAS 2013, Durham, NC, 2013, http://uspas.fnal.gov/materials/materials-table.shtml.

[22] G. Ciovati, Cavity fabrication, lecture at USPAS 2015, http://uspas.fnal.gov/materials/15Rutgers/Cavity_Fabrication.pdf.

[23] D. Proch, RF Cavities fabrication, in Proceedings of the CAS–CERN Accelerator School, Superconductivity and Cryogenics for Accelerators and Detectors, Erice, 2002, CERN 2004-008 (CERN, Geneva, 2004), p. 214. http://cdsweb.cern.ch/record/503603/files/CERN-2004-008.pdf.

[24] D. Alesini *et al.*, *Nucl. Instrum. Meth. A* **580**(3) (2007) 1176. https://doi.org/10.1016/j.nima.2007.06.045

[25] C. Steele, *IEEE T. Microw. Theory* **14**(2) (1966) 70. https://doi.org/10.1109/TMTT.1966.1126168

[26] D. Alesini *et al.*, *Nucl. Instrum. Methods Phys. Res., Sect. A* **837** (2016) 161. https://doi.org/10.1016/j.nima.2016.09.010

[27] D.Alesini *et al.*, *J. Instrum.* **8** (2013) P10010. https://dx.doi.org/10.1088/ 1748-0221/8/10/P10010.

[28] F. Cardelli, PhD thesis, Sapienza Università di Roma, 2017.

[29] J.K. Sekutowicz, Superconducting elliptical cavities, in Proceedings of the CERN Accelerator School RF for Accelerators, Ebeltoft, Denmark 8–17 June, 2010, CERN–2011–007 (CERN, Geneva, 2011), p. 369. http://cas.web.cern.ch/schools/ebeltoft-2010.

[30] J. Sekutowicz, Superconducting linear accelerator for the European XFEL, presentation at the International Workshop on X-ray Diagnostics and Scientific Application of the European XFEL, Ryn, Poland, 2010.

http://xfel-old.desy.de/sites/site_xfel-gmbh/content/e63594/e63599/e81230/e70177/e83636/ryn-workshop-2010-sekutowicz_eng.pdf

[31] R.F. Parodi, Couplers and HOM dampers, in Proceedings of the CAS–CERN Accelerator School, Superconductivity and Cryogenics for Accelerators and Detectors, Erice, 2002, CERN 2004-008 (CERN, Geneva, 2004), p. 253. http://cdsweb.cern.ch/record/503603/files/CERN-2004-008.pdf.

[32] P. Michelato, Cavity processing: EP/BCP, heat treatments, baking and clean room techniques, presentation at SRF2013, Caen/Paris, September 19-27, 2013. https://indico.in2p3.fr/event/9782/contributions/50504/.

[33] G. Ciovati, Surface preparation, lecture at USPAS Accelerator School, 2015, http://uspas.fnal.gov/materials/15Rutgers/Surface_Preparation.pdf.

[34] D. Alesini *et al.*, Realization and high power tests of damped C-band accelerating structures for the ELI-NP linac, in proceeding of IPAC 2016, Busan, Korea, 2016, (Jacow, CERN, Gedneva, 2016) p. 399.

[35] G. Ciovati, Cavity limitations, lecture at USPAS Accelerator School, June 2015, http://uspas.fnal.gov/materials/15Rutgers/Cavity_Limitations.pdf.

[36] D. Dowell, High brightness electron injectors for light sources, lecture at USPAS School, 2010, http://uspas.fnal.gov/materials/10MIT/MIT-High-Brightness.shtml.

[37] D. Alesini *et al.*, High power test results of the ELI-NP S-band gun fabricated with the new clamping technology without brazing, in Proceeding of IPAC 2017, Copenhagen, Denmark, 2017, (Jacow, CERN, Gedneva, 2017), p. 3662.

[38] D.H. Dowell *et al.*, Results of the SLAC LCLS gun high-power RF tests, in proceeding of PAC07, Albuquerque, New Mexico, 2007, (IEEE, 2007) p. 1296. https://doi.org/10.1109/PAC.2007.4441061

[39] C. Limborg *et al.*, RF design of the LCLS Gun, LCLS-TN-05-3, 2005. http://www-ssrl.slac.stanford.edu/lcls/technotes/LCLS-TN-05-3.pdf.

[40] L. Xiao *et al.*, Dual feed RF gun design for the LCLS, in Proceedings of the 2005 Particle Accelerator Conference, Knoxville, Tennessee, 2005, (IEEE 2005) p. 3432.

https://doi.org/10.1109/PAC.2005.1591495

[41] B. Dwersteg *et al.*, *Nucl. Instrum. Meth. A* **393**(1–3) (1997) 93–95. https://doi.org/10.1016/S0168-9002(97)00434-8

[42] F. Stephan *et al.*, *Phys. Rev. ST Accel. Beams* **13**(12) (2010) 020704. https://doi.org/10.1103/PhysRevSTAB.13.020704

[43] C. Gulliford *et al.*, *Phys. Rev. ST Accel. Beams* **16**(7) (2013) 073401. https://doi.org/10.1103/PhysRevSTAB.16.073401

[44] R.G. Carter, Review of RF power sources for particle accelerators, in Proceedings of the CAS–CERN Accelerator School, Radio Frequency Engineering, Seeheim, Germany, 8–16 May 2000, CERN 2005-003 (CERN, Geneva, 2005), p. 107. http://cdsweb.cern.ch/record/386544/files/CERN-2005-003.pdf.

[45] R.G. Carter, RF power generation, in Proceedings of the CERN Accelerator School RF for accelerators, Ebeltoft, Denmark 8–17 June 2010, CERN-2011-007 (CERN, Geneva, 2011), p. 173. http://dx.doi.org/10.5170/CERN-2011-007.

[46] R.K. Cooper and R.G. Carter, High-power RF transmission, in Proceedings of the CAS–CERN Accelerator School: Radio Frequency Engineering, Seeheim, Germany, 8–16 May 2000, CERN 2005-003 (CERN, Geneva, 2005), p. 210. http://cdsweb.cern.ch/record/386544/files/CERN-2005-003.pdf.

[47] Z. Farkas *et al.*, *IEEE Trans. Nucl. Sci.*, **22**(3) (2007) 1299. https://doi.org/10.1109/TNS.1975.4327871